SIAM J. IMAGING SCIENCES
Vol. 5, No. 3, pp. 769–808

Passive Imaging of Moving Targets Using Sparse Distributed Apertures*

Ling Wang† and Birsen Yazici‡

Abstract. We develop a new passive imaging method for moving targets in free space using measurements from a sparse array of receivers that rely on illumination sources of opportunity. Our imaging method consists of a novel passive measurement model for moving targets and an associated image formation method. The passive measurement model for moving targets relates measurements at a given receiver to measurements at other receivers in terms of Doppler and delay based on the physics of wave propagation as well as the statistics of noise. Next, we use this model to address the image formation as a generalized likelihood ratio test for an unknown target position and velocity. The image is formed by using the position- and velocity-resolved test-statistic that is obtained by maximizing the signal-to-noise ratio of the test-statistic. When the discriminant functional is constrained to be linear, the test-statistic can be viewed as the superposition of the filtered, scaled, and delayed correlations of the measurements obtained at different receivers. We analyze the spatial and velocity resolution of the four-dimensional point spread function of our imaging method in terms of the number of receivers and transmitters and the nature of the waveforms of opportunity. We present extensive numerical simulations to demonstrate the performance of our passive moving target imaging method for different numbers of receivers and different types of waveforms of opportunity available in the real world.

Key words. passive radar, imaging, moving targets, distributed apertures, generalized likelihood ratio test

AMS subject classification. 78A46

DOI. 10.1137/11084368X

1. Introduction.

1.1. Motivation and overview of our approach.

With the rapid growth of broadcasting stations, mobile phone base stations, communication and navigation satellites, as well as the relatively low cost and rapid deployment of receivers, passive radar imaging using transmitters of opportunity has emerged as an active area of research in recent years [1, 10, 11, 12, 13, 14, 17, 23, 24, 25, 26, 27, 28, 29, 34, 36, 41, 42, 45, 47, 50, 51, 52, 53]. The transmitters of opportunity could be cooperative where the information regarding the location, waveform, or bandwidth of the sources is available or noncooperative where no such information is available.

In this paper, we present a new imaging method to determine the distribution of moving targets in position and velocity spaces in free space using a sparse array of receivers and noncooperative transmitters of opportunity. We assume that the receivers are arbitrarily distributed

*Received by the editors August 8, 2011; accepted for publication (in revised form) March 15, 2012; published electronically July 3, 2012. This work was supported by the Air Force Office of Scientific Research (AFOSR) under the agreements FA9550-07-1-0363 and FA9550-09-1-0013 and by the National Science Foundation (NSF) under grant CCF-08030672.
http://www.siam.org/journals/siims/5-3/84368.html
†Department of Information and Communication Engineering, Nanjing University of Aeronautics and Astronautics, Nanjing 210016, China (wanglrpi@gmail.com).
‡Department of Electrical, Computer and Systems Engineering, Rensselaer Polytechnic Institute, Troy, NY 12180 (yazici@ecse.rpi.edu).

in space that are several hundred wavelengths apart. We refer to such an array as a distributed aperture. We assume that the location and beampatterns of the transmitters of opportunity, as well as the transmitted waveforms, are unknown. We introduce a self-consistent theoretical framework based on physics-based modeling and estimation-detection theory. Within this framework our imaging method consists of a novel passive measurement model and an associated image formation method. The new passive measurement model relates the Doppler as well as delay information measured at a receiver location to the delay and Doppler information measured at other receiver locations due to a hypothetical moving target in position and velocity spaces. We use the new passive measurement model to address the moving target imaging problem as a position- and velocity-resolved binary hypothesis test, which has its roots in the generalized likelihood ratio test (GLRT) [31, 32]. We use the position- and velocity-resolved test-statistics produced by the hypothesis testing to form an image in position and velocity spaces. We determine the test-statistic by maximizing its signal-to-noise ratio (SNR) while constraining the associated discriminant functional to be linear. The resulting test-statistic can be viewed as a superposition of filtered, delayed, and scaled (or dilated) correlations of measurements at different receivers. While the GLRT approach can accommodate arbitrary probability density function models, the choice of the linear discriminant functional results in an explicit test-statistic and allows us to readily perform resolution analysis in terms of the point spread function of our imaging method. We analyze the resolution of the reconstructed images under different imaging scenarios including different numbers of transmitters and receivers and different types of transmitted waveforms. Our analysis shows that the resolution of position and velocity is determined by the intersection of the four- (or six-)dimensional passive-iso-Doppler and passive-iso-range manifolds introduced in this paper, whose spread is associated with the underlying Doppler and range ambiguity functions of the transmitted waveforms of opportunity. We analyze the computational complexity of our passive moving target imaging algorithms and present extensive numerical simulations to demonstrate the performance of our imaging method using different waveforms of opportunity available in the real world.

1.2. Related work and advantages of our approach. A number of passive moving target detection and imaging approaches have been presented in the literature [1, 12, 13, 14, 17, 23, 24, 25, 26, 27, 29, 34, 36, 41, 42, 45, 50, 51]. With the exception of [36], these works either assume a priori knowledge of the transmitter related information or estimate this information from measurements. The works in [1, 12, 13, 14, 17, 23, 24, 25, 26, 27, 29, 34, 36, 41, 42, 45] mainly focus on the detection of moving targets in a bistatic framework [54]. In [50] a method based on the inverse Fourier transform and interpolation was presented for imaging of airborne targets. The method uses a single receiver and multiple television transmitters, which can be viewed as a multistatic inverse synthetic aperture radar imaging technique [6, 43]. The paper [51] is an advancement over [50], where the Fourier transform along the cross-range dimension is replaced by the smoothed pseudo-Wigner–Ville distribution to address the aspect angle dependent variability in target reflectivity.

In [36], a passive detection technique for moving targets which exploits target thermal radiation was considered. This method is based on the cross-correlation of measurements from two different locations over a temporal window. The range and Doppler properties were

analyzed, and several limitations of the approach including difficulties due to noise and clutter and selection of the temporal window were presented.

The technique of cross-correlation of measurements was also used in passive synthetic aperture radar (SAR) imaging [52, 53] and other passive imaging applications [3, 4, 16, 18, 19, 20, 40, 47]. The correlation processing eliminates the need for knowledge about the transmitter location and waveform. As a result it is applicable to passive imaging problems using noncooperative sources of opportunity. Our present work falls into this class of approaches. However, our method arises from a different consideration from those described in [3, 4, 16, 18, 19, 20, 40]. In our current and previous works [47], we have introduced a new, self-consistent theoretical framework for passive imaging based on physics-based modeling and estimation-detection theory. Our theory results in a cross-correlation–based approach only under certain design constraints.

In [53] we developed a delay-based correlation processing combined with a filtered-backprojection technique to form high resolution SAR images of ground radiance. This technique is particularly suitable for wideband illumination sources of opportunity. In [52], we developed a scaling-and-delay–based correlation combined with a filtered-backprojection technique to recover the ground radiance using ultranarrowband illumination sources of opportunity. Both of these works address imaging of a stationary scene in free space. The delay-based correlation was also studied in [3, 4, 16, 18, 19, 20, 40] to image stationary heterogeneities in the context of geophysical imaging both in free space as well as in multiple scattering environments.

In [47] we reported a novel passive imaging method using sparse distributed apertures. This method assumes that the targets are at rest during the transmission and the corresponding reception and focuses on the reconstruction of the distribution of targets in the *position space only*. This work, as well as an earlier work by one of the authors, introduces the hypothesis-testing–based approach to imaging [46]. In all of these works [3, 4, 16, 18, 19, 20, 40, 47], imaging of stationary targets was considered. In this paper, we consider the problem of passive imaging of moving targets using sparse distributed apertures to reconstruct the distribution of targets in *both position and velocity spaces*. The method exploits the Doppler information induced by the motion of the moving targets as well as the statistics of the additive noise. In [48, 49], we presented conference versions of the present paper without many of the results, derivations, and analysis.

Our approach has a number of advantages as compared to the existing passive imaging or detection methods for moving targets: (1) Unlike the existing methods that focus on the detection of the radial velocity of the moving target [1, 12, 13, 14, 17, 23, 24, 25, 26, 27, 29, 34, 36, 41, 42, 45] using specific waveforms available in the real world or target radiation, our approach determines the two- or three-dimensional velocity information as well as the two- or three-dimensional position of targets. (2) As compared to the existing passive radar detection methods, our approach does not require transmitters or receivers with high directivity. (3) Our approach is applicable to both cooperative and noncooperative transmitters of opportunity. (4) For ease of exposition, we focus on the passive imaging of deterministic moving targets with measurements embedded in thermal noise. However, our approach can be easily extended to passive imaging of statistical targets embedded in random clutter.

While our treatment focuses primarily on radar imaging, our method is directly applicable to passive imaging of moving objects in seismic, acoustic, or microwave imaging. Additionally,

our physics-based modeling approach may allow extension of our method to imaging of moving targets in multiple scattering environments with applications in urban imaging and imaging of underground structures [37, 38].

1.3. Organization of the paper. The rest of our paper is organized as follows: In section 2, we describe the models for a moving target and incident and scattered fields and next use these to develop a passive measurement model for moving targets. In section 3, we use the passive measurement model developed in section 2 and address the moving target imaging problem within the GLRT framework. In section 4, we present the resolution analysis of our imaging method in position and velocity spaces. In section 5, we present the computational complexity analysis of our imaging method. In section 6, we present numerical simulations. Section 7 concludes our discussion. The paper includes two appendices: Appendix A includes the derivation of the optimal linear discriminant functional used for passive image formation. Appendix B includes the derivation of an intermediate result used in section 3.

2. Passive measurement model for moving targets. In this section, we first describe the models for the moving target and incident and scattered fields and next use these models to develop a measurement model for passive imaging of moving targets in free space.

Table 1 lists notation used throughout the paper. The bold $\mathbf{x}$ denotes a variable in three-dimensional Euclidean space and the italic bold $\boldsymbol{x}$ denotes a variable in two-dimensional space. The operators are denoted with calligraphic letters—for example, $\mathcal{K}, \mathcal{G}, \mathcal{P}$, etc. For a function f, $\hat{f}$ denotes its Fourier transform and f^* denotes its complex conjugate.

2.1. Models for moving target, incident, and scattered fields. The propagation of each component of electromagnetic waves due to an arbitrary source distribution $s(\mathbf{x}, t)$ in a medium can be described using the scalar wave equation [2, 15, 22]:

$$[\nabla^2 - c^{-2}(\mathbf{x}, t)\partial_t^2]E(\mathbf{x}, t) = s(\mathbf{x}, t), \tag{2.1}$$

where c is the wave speed in the medium and E is the electric field. We assume that moving scatterers are embedded in free space. Let c_0 denote the speed of light in free space and g be the *Green's function* satisfying

$$[\nabla^2 - c_0^{-2}\partial_t^2]g(\mathbf{x}, \mathbf{z}, t) = \delta(\mathbf{x} - \mathbf{z})\delta(t). \tag{2.2}$$

The wave speed c in moving scatterers can be expressed in terms of the background propagation speed and the perturbation due to deviation from the background reflectivity. Let $q_{\mathbf{v}}$ denote the *phase-space* distribution, at time $t = 0$, of scatterers moving with velocity $\mathbf{v}$. The moving scatterers in the spatial volume d^3x (at $\mathbf{x}$) give rise to [8]

$$c^{-2}(t, \mathbf{x}) = c_0^{-2} + \int q_{\mathbf{v}}(\mathbf{x} - \mathbf{v}t)d\mathbf{v}. \tag{2.3}$$

We assume that the electromagnetic waves decay rapidly as they penetrate the ground [7]. We then write $q_{\mathbf{v}}(\mathbf{x}-\mathbf{v}t)$ in terms of the two-dimensional location and two-dimensional velocity as follows:

$$q_{\mathbf{v}}(\mathbf{x} - \mathbf{v}t) = q_{\boldsymbol{v}}(\boldsymbol{x} - \boldsymbol{v}t)\delta(x_3 - h(\boldsymbol{x}))\delta(v_3 - Dh(\boldsymbol{x}) \cdot \boldsymbol{v}), \tag{2.4}$$

Table 1
Table of notation.

Symbol	Designation	Symbol	Designation
c_0	Speed of light in free space	$s(\mathbf{x},t)$	Source at location $\mathbf{x}$ and time t
$g(\mathbf{x},\mathbf{y},t)$	Green's function of a homogeneous medium representing the field at location $\mathbf{x}$ and time t due to an impulsive source at location $\mathbf{y}$ at time zero	$q_{\mathbf{v}}(\mathbf{x})$	Phase-space distribution of scatters located at $\mathbf{x}$ moving with velocity $\mathbf{v}$
E^{in}	The incident field	E^{sc}	The scattered field
$\tilde{E}^{\text{in}}$	The incident field observed by the moving target	E_q^{in}	The incident field due to the qth transmitter located at $\mathbf{z}_q$
p_q	Transmitted waveform by the qth transmitter	$T_{\mathbf{z}_q}$	Time at which the transmission starts from location $\mathbf{z}_q$
ρ	Reflectivity of a point target	$\mathbf{x}_i$	Location of the ith receiver
$\hat{m}_i$	Fourier transform of the measurement at the ith receiver	$\hat{n}_i$	Additive white thermal noise at the ith receiver
$\mu_{\boldsymbol{y},\boldsymbol{v},i}$	Doppler-scale-factor observed by the ith receiver	$\tilde{\mu}_{\boldsymbol{y},\boldsymbol{v},\mathbf{z}_q}$	Doppler-scale-factor observed by the target due to the radial movement relative to the qth transmitter
$\alpha_{\boldsymbol{y},\boldsymbol{v},\mathbf{x}_i,\mathbf{z}_q}$	Doppler-scale-factor observed by the ith receiver due to a transmission from $\mathbf{z}_q$ and a target located at $\boldsymbol{y}$ moving with velocity $\boldsymbol{v}$	$\gamma_{\boldsymbol{y},\boldsymbol{v},ij}$	Passive Doppler-scale-factor with respect to the ith and jth receivers due to a target located at $\boldsymbol{y}$ moving with velocity $\boldsymbol{v}$
$\mathcal{P}_{\boldsymbol{y},\boldsymbol{v},i}$	Forward-propagation operator mapping the incident field from $\boldsymbol{y}$ on a moving target with velocity $\boldsymbol{v}$ to the ith receiver located at $\mathbf{x}_i$	$\mathcal{P}^{-1}_{\boldsymbol{y},\boldsymbol{v},i}$	Back-propagation operator mapping the ith measurement to a hypothetical target located at $\boldsymbol{y}$ moving with a hypothetical velocity $\boldsymbol{v}$
$\mathcal{S}_{\boldsymbol{v},i}$	Scaling operator that accounts for the Doppler scaling effect observed by the ith receiver	$\mathcal{G}_{\boldsymbol{y},i}$	Operator that accounts for the wave propagation in the stationary background from the target to the ith receiver
$\mathbf{P}_{\boldsymbol{y},\boldsymbol{v}}$	Diagonal matrix with elements $\mathcal{P}_{\boldsymbol{y},\boldsymbol{v},i}\mathcal{P}^{-1}_{\boldsymbol{y},\boldsymbol{v},j}$, $i=1,\dots,N$, and $i\neq j$ for some $1\le j\le N$	$\mathbf{m}$	Measurement vector (see (2.40))
$\mathbf{m_r}$	Reference measurement vector (see (2.41))	$\mathbf{n}$	Noise vector (see (2.42))
$\mathbf{R_n}$	Autocovariance matrix of $\mathbf{n}$	$\mathbf{w}$	Template of the linear detector
S_n^i	Power spectral density function of the noise at the ith receiver	K	Point spread function of the imaging operator
$\lambda(\boldsymbol{y},\boldsymbol{v})$	Test-statistic at position $\boldsymbol{y}$ and velocity $\boldsymbol{v}$	SNR_λ	SNR of the test-statistic

where $\mathbf{x}=(\boldsymbol{x},x_3),\boldsymbol{x}\in\mathbb{R}^2$, and $\mathbf{v}=(\boldsymbol{v},v_3),\boldsymbol{v}\in\mathbb{R}^2$, $h:\mathbb{R}^2\to\mathbb{R}$ represents the ground topography, and $Dh(\boldsymbol{x})=[\frac{\partial h}{\partial x_1}\quad\frac{\partial h}{\partial x_2}]$.

Let E^{sc} denote the scattered field due to the moving perturbation $q_{\boldsymbol{v}}$. Then, under the

Born approximation [39], the scattered field is modeled as[1]

$$E^{\text{sc}}(\mathbf{x},t)=\int g(\mathbf{x},\boldsymbol{y},t-\tau)q_{\boldsymbol{v}}(\boldsymbol{y}-\boldsymbol{v}\tau)\partial_\tau^2 E^{\text{in}}(\boldsymbol{y},\tau)d\tau d\boldsymbol{y}d\boldsymbol{v}, \tag{2.5}$$

where $g(\mathbf{x},\boldsymbol{y},t)$ is the three-dimensional free space Green's function equal to $g(\mathbf{x},(\boldsymbol{y},h(\boldsymbol{y})),t)$. E^{in} denotes the incident field due to the source distribution $s(\mathbf{x},t)$ modeled as

$$E^{\text{in}}(\boldsymbol{y},t)=\int g(\boldsymbol{y},\mathbf{z},t-\tau)s(\mathbf{z},\tau)d\tau d\mathbf{z}, \tag{2.6}$$

where $g(\boldsymbol{y},\mathbf{z},t)$ is the three-dimensional Green's function defined as $g((\boldsymbol{y},h(\boldsymbol{y})),\mathbf{z},t)$.

For multiple transmitters with isotropic antennas, say, M, the source distribution becomes

$$s(\mathbf{x},t)=\sum_{q=1}^{M}\delta(\mathbf{x}-\mathbf{z}_q)p_q(t+T_{\mathbf{z}_q}), \tag{2.7}$$

where $\mathbf{z}_q, q=1,\dots,M$, denotes the location of the qth transmitter transmitting the waveform $\hat{p}_q$ starting at time $t=T_{\mathbf{z}_q}$.

Note that the isotropic antenna assumption is not necessary for the rest of our development. The following models can be extended to incorporate realistic antenna models in a straightforward manner. However, this assumption is made to simplify the rest of our discussion.

Substituting (2.7) into (2.6), we have

$$E^{\text{in}}(\boldsymbol{y},t)=\sum_{q=1}^{M}\int \underbrace{g(\boldsymbol{y},\mathbf{z}_q,t-\tau)p_q(\tau+T_{\mathbf{z}_q})}_{E_q^{\text{in}}(\boldsymbol{y},\mathbf{z}_q,t)}d\tau, \tag{2.8}$$

where E_q^{in} represents the incident field on the target due to the qth transmitter.

Performing the change of variables $\boldsymbol{y}'=\boldsymbol{y}-\boldsymbol{v}\tau$, (2.5) becomes

$$E^{\text{sc}}(\mathbf{x},t)=\int g(\mathbf{x},\boldsymbol{y}'+\boldsymbol{v}\tau,t-\tau)q_{\boldsymbol{v}}(\boldsymbol{y}')\partial_\tau^2 E^{\text{in}}(\boldsymbol{y}'+\boldsymbol{v}\tau,\tau)d\tau d\boldsymbol{y}'d\boldsymbol{v}, \tag{2.9}$$

where $E^{\text{in}}(\boldsymbol{y}'+\boldsymbol{v},\tau)$ is given in (2.6) with $\boldsymbol{y}$ replaced by $\boldsymbol{y}'+\boldsymbol{v}\tau$.

For free space, the *Green's function* is given by

$$g(\mathbf{x},\mathbf{z},t)=\frac{\delta(t-|\mathbf{x}-\mathbf{z}|/c_0)}{4\pi|\mathbf{x}-\mathbf{z}|}. \tag{2.10}$$

Under the slow-mover assumption,[2] we approximate

$$\begin{aligned}|\mathbf{x}-(\mathbf{y}+\mathbf{v}\tau)| &\approx |\mathbf{x}-\mathbf{y}|-\widehat{\mathbf{x}-\mathbf{y}}\cdot\mathbf{v}\,\tau,\\ |(\mathbf{y}+\mathbf{v}\tau)-\mathbf{z}_q| &\approx |\mathbf{y}-\mathbf{z}_q|+\widehat{\mathbf{y}-\mathbf{z}_q}\cdot\mathbf{v}\,\tau.\end{aligned} \tag{2.11}$$

[1] Note that the scattered field can also be derived from the perspective of scattering theory [9], which leads to another expression where the double derivative with respect to τ can be removed in (2.5) under the assumption that the target reflectivity is in the "optical region," i.e., independent of frequency ω.

[2] The speed of the target, $|\boldsymbol{v}|$, is much slower than the speed of light, c_0, or $|\boldsymbol{v}|t$ is much less than the distance between the receiver (transmitter) and the target.

Thus, we have

$$g(\mathbf{x}, \boldsymbol{y} + \boldsymbol{v}\tau, t) \approx g\left(\mathbf{x}, \boldsymbol{y}, t + \frac{\widehat{\mathbf{x}-\mathbf{y}}\cdot\mathbf{v}}{c_0}\tau\right), \tag{2.12}$$

$$g(\boldsymbol{y} + \boldsymbol{v}\tau, \mathbf{z}, \tau) \approx g\left(\boldsymbol{y}, \mathbf{z}, (1 - \frac{\widehat{\mathbf{y}-\mathbf{z}}\cdot\mathbf{v}}{c_0})\tau\right). \tag{2.13}$$

Note that $\mathbf{y} = (\boldsymbol{y}, h(\boldsymbol{y}), t)$ and $\mathbf{v} = (\boldsymbol{v}, Dh(\boldsymbol{y})\cdot\boldsymbol{v})$.

Using (2.12), (2.13), and (2.6) and replacing $\boldsymbol{y}'$ with $\boldsymbol{y}$ in (2.9), we obtain

$$E^{\mathrm{sc}}(\mathbf{x}, t) = \int g(\mathbf{x}, \boldsymbol{y}, t - \mu_{\boldsymbol{y},\boldsymbol{v},\mathbf{x}}\tau) q_{\boldsymbol{v}}(\boldsymbol{y}) \partial_\tau^2 \tilde{E}^{\mathrm{in}}(\boldsymbol{y}, \tau) d\tau d\boldsymbol{y} d\boldsymbol{v}, \tag{2.14}$$

where

$$\tilde{E}^{\mathrm{in}}(\boldsymbol{y}, \tau) = \sum_{q=1}^{M} E_q^{\mathrm{in}}(\mathbf{y}, \mathbf{z}_q, \tilde{\mu}_{\boldsymbol{y},\boldsymbol{v},\mathbf{z}_q}\tau) \tag{2.15}$$

with

$$E_q^{\mathrm{in}}(\boldsymbol{y}, \mathbf{z}_q, \tilde{\mu}_{\boldsymbol{y},\boldsymbol{v},\mathbf{z}_q}\tau) = \int g(\mathbf{y}, \mathbf{z}_q, \tilde{\mu}_{\boldsymbol{y},\boldsymbol{v},\mathbf{z}_q}\tau - \tau') p(\tau' + T_{\mathbf{z}_q}) d\tau' \tag{2.16}$$

and

$$\mu_{\boldsymbol{y},\boldsymbol{v},\mathbf{x}} = 1 + \frac{\widehat{\mathbf{y}-\mathbf{x}}\cdot\mathbf{v}}{c_0}, \tag{2.17}$$

$$\tilde{\mu}_{\boldsymbol{y},\boldsymbol{v},\mathbf{z}_q} = 1 - \frac{\widehat{\mathbf{y}-\mathbf{z}_q}\cdot\mathbf{v}}{c_0}. \tag{2.18}$$

As compared to (2.6), which presents the incident field on a static target, (2.15) defines the incident field observed by a moving target with velocity $\boldsymbol{v}$ due to transmitters located at $\mathbf{z}_q, q = 1, \ldots, M$, which accounts for the Doppler scaling effect induced by the movement of the target.

Note that the scale factor, $\tilde{\mu}_{\boldsymbol{y},\boldsymbol{v},\mathbf{z}_q}$, in (2.18) accounts for the Doppler scaling effect induced by the movement of the target on the field at $\boldsymbol{y}$ due to a source located at $\mathbf{z}_q$. We refer to $\tilde{\mu}_{\boldsymbol{y},\boldsymbol{v},\mathbf{z}_q}$ as the *Doppler-scale-factor observed by the moving target* located at $\boldsymbol{y}$ moving with velocity $\boldsymbol{v}$ due to a waveform transmitted from $\mathbf{z}_q$. The scale factor, $\mu_{\boldsymbol{y},\boldsymbol{v},\mathbf{x}}$, in (2.17) accounts for the Doppler scaling effect observed at the receiver location $\mathbf{x}$ due to a moving target with velocity $\boldsymbol{v}$. We refer to $\mu_{\boldsymbol{y},\boldsymbol{v},\mathbf{x}}$ as the *Doppler-scale-factor observed at location* $\mathbf{x}$ *due to a moving target* with velocity $\boldsymbol{v}$ at location $\boldsymbol{y}$. In the discussion that follows, we focus on the slow-mover case.

Using (2.14), the measurement at the receiver located at $\mathbf{x}_0$ contaminated with additive thermal noise $n(t)$ can be modeled as

$$m(t) = \int g(\mathbf{x}_0, \boldsymbol{y}, t - \mu_{\boldsymbol{y},\boldsymbol{v},\mathbf{x}}\tau) q_{\boldsymbol{v}}(\boldsymbol{y}) \partial_\tau^2 \tilde{E}^{\mathrm{in}}(\boldsymbol{y}, \tau) d\tau d\boldsymbol{y} d\boldsymbol{v} + n(t). \tag{2.19}$$

We assume that $n(t)$ is zero-mean with finite second-order statistics.

In the Fourier domain, (2.19) becomes

$$\hat{m}(\omega) = \int \hat{g}(\mathbf{x}_0, \boldsymbol{y}, \omega) q_{\boldsymbol{v}}(\boldsymbol{y}) \mu_{\boldsymbol{y},\boldsymbol{v},\mathbf{x}_0} \omega^2 \hat{\tilde{E}}^{\text{in}}(\boldsymbol{y}, \mu_{\boldsymbol{y},\boldsymbol{v},\mathbf{x}_0}\omega) d\boldsymbol{y} d\boldsymbol{v} + \hat{n}(\omega), \tag{2.20}$$

where $\hat{g}(\mathbf{x}_0, \boldsymbol{y}, \omega)$ denotes the Fourier transform of the three-dimensional free space Green's function $g(\mathbf{x}_0, (\boldsymbol{y}, h(\boldsymbol{y})), t)$ given in (2.10), i.e.,

$$\hat{g}(\mathbf{x}_0, \boldsymbol{y}, \omega) = \frac{\mathrm{e}^{-\mathrm{i}\frac{\omega}{c_0}|\mathbf{x}_0 - \mathbf{y}|}}{4\pi|\mathbf{x}_0 - \mathbf{y}|}, \tag{2.21}$$

and

$$\hat{\tilde{E}}^{\text{in}}(\boldsymbol{y}, \omega) = -\sum_{q=1}^{M} \frac{1}{\tilde{\mu}^2_{\boldsymbol{y},\boldsymbol{v},\mathbf{z}_q}} \hat{E}^{\text{in}}_q \left(\boldsymbol{y}, \mathbf{z}_q, \frac{\omega}{\tilde{\mu}_{\boldsymbol{y},\boldsymbol{v},\mathbf{z}_q}} \right) \tag{2.22}$$

with $\hat{E}^{\text{in}}_q(\omega, \boldsymbol{y}, \mathbf{z})$ denoting the Fourier transform of (2.16), i.e.,

$$\hat{E}^{\text{in}}_q \left(\boldsymbol{y}, \mathbf{z}_q, \frac{\omega}{\tilde{\mu}_{\boldsymbol{y},\boldsymbol{v},\mathbf{z}_q}} \right) = \frac{1}{\tilde{\mu}_{\boldsymbol{y},\boldsymbol{v},\mathbf{z}_q}} \hat{g} \left(\mathbf{y}, \mathbf{z}, \frac{\omega}{\tilde{\mu}_{\boldsymbol{y},\boldsymbol{v},\mathbf{z}_q}} \right) \hat{p}_q \left(\frac{\omega}{\tilde{\mu}_{\boldsymbol{y},\boldsymbol{v},\mathbf{z}_q}} \right) \mathrm{e}^{\mathrm{i}\frac{\omega}{\tilde{\mu}_{\boldsymbol{y},\boldsymbol{v},\mathbf{z}_q}} T_{\mathbf{z}_q}}. \tag{2.23}$$

Note that since the waveform $\hat{p}$ is typically band-limited, we restrict our analysis to some range of ω.

Substituting (2.23) into (2.22) and the result back into (2.20), and using (2.21), we obtain

$$\begin{aligned} \hat{m}(\omega) = \frac{-\omega^2}{(4\pi)^2} \sum_{q=1}^{M} \int & \frac{\mathrm{e}^{\mathrm{i}\phi_{\boldsymbol{y},\boldsymbol{v},\mathbf{x}_0,\mathbf{z}_q}}}{|\mathbf{y} - \mathbf{x}_0||\mathbf{y} - \mathbf{z}_q| \alpha^3_{\boldsymbol{y},\boldsymbol{v},\mathbf{x}_0,\mathbf{z}_q}} \\ & \times \hat{p}_q \left(\frac{\omega}{\alpha_{\boldsymbol{y},\boldsymbol{v},\mathbf{x}_0,\mathbf{z}_q}} \right) q_{\boldsymbol{v}}(\boldsymbol{y}) d\boldsymbol{y} d\boldsymbol{v} + \hat{n}(\omega), \end{aligned} \tag{2.24}$$

where

$$\phi_{\boldsymbol{y},\boldsymbol{v},\mathbf{x}_0,\mathbf{z}_q} = \frac{\omega}{\alpha_{\boldsymbol{y},\boldsymbol{v},\mathbf{x}_0,\mathbf{z}_q}} \left(T_{\mathbf{z}_q} - \frac{|\mathbf{y} - \mathbf{z}_q|}{c_0} \right) - \omega \frac{|\mathbf{y} - \mathbf{x}_0|}{c_0} \tag{2.25}$$

and

$$\alpha_{\boldsymbol{y},\boldsymbol{v},\mathbf{x}_0,\mathbf{z}_q} = \frac{\tilde{\mu}_{\boldsymbol{y},\boldsymbol{v},\mathbf{z}_q}}{\mu_{\boldsymbol{y},\boldsymbol{v},\mathbf{x}_0}} = \frac{1 - \widehat{\mathbf{y} - \mathbf{z}_q} \cdot \mathbf{v}/c_0}{1 + \widehat{\mathbf{y} - \mathbf{x}_0} \cdot \mathbf{v}/c_0}. \tag{2.26}$$

Since the scale factor $\alpha_{\boldsymbol{y},\boldsymbol{v},\mathbf{x}_0,\mathbf{z}_q}$ accounts for the Doppler scaling effect on the scattered-field measurements due to the qth transmitter induced by the the movement of the target, we refer to $\alpha_{\boldsymbol{y},\boldsymbol{v},\mathbf{x}_0,\mathbf{z}_q}$ as the *Doppler-scale-factor* with respect to the qth transmitter.

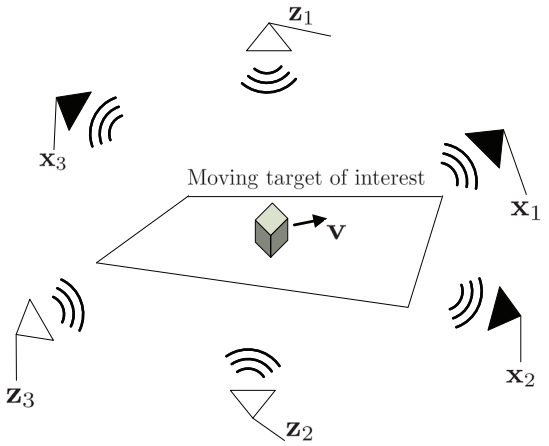

Figure 1. *An illustration of the imaging scenario using distributed apertures. The black triangles denote the receivers, and the white triangles denote the transmitters. The arrow shows the velocity vector of the target.*

2.2. A measurement model for passive imaging of moving targets using distributed apertures. In the analysis that follows, we consider N receivers located at $\mathbf{x}_i\,, i = 1, \ldots, N$, and M transmitters located at $\mathbf{z}_q, q = 1, \ldots, M$. The receivers and transmitters are arbitrarily located several hundred wavelengths apart with known receiver locations but unknown transmitter locations. Furthermore, we assume that there is a common reference clock for all receivers. This common reference clock allows coherent data processing. Figure 1 illustrates the imaging scenario that is considered.

For the rest of our development we assume that the phase-space distribution $q_{\boldsymbol{v}}(\boldsymbol{y})$ is deterministic. This assumption allows us to simplify the analysis and distill the important aspects of our imaging theory. The results can be easily extended to statistical targets embedded in clutter.

For active imaging, measurements are expressed in terms of the transmitted waveforms and the location of the transmitters as in (2.24). However, for noncooperative passive detection and imaging applications, such information is not available. Therefore, we develop a passive measurement model that expresses measurements at each receiver in terms of the measurements at a different receiver. The model is based on the fact that the measurements at all receivers are due to the same incident field $\tilde{E}^{\text{in}}$, target velocity, and phase-space distribution. The model involves back-propagating the measurement at a receiver location to a hypothetical target location moving with a hypothetical velocity and then forward-propagating the resulting field to another receiver location.

Using (2.20), we define the forward-propagation operator, $\mathcal{P}_{\boldsymbol{y},\boldsymbol{v},i}$, with respect to the ith receiver as a linear operator expressed as

$$\mathcal{P}_{\boldsymbol{y},\boldsymbol{v},i}[u](\omega) = \mathcal{G}_{\boldsymbol{y},i}\mathcal{S}_{\boldsymbol{v},i}[u](\omega), \tag{2.27}$$

where

$$u(\boldsymbol{y},\boldsymbol{v},\omega) = q_{\boldsymbol{v}}(\boldsymbol{y})\omega^2\hat{\tilde{E}}^{\text{in}}(\boldsymbol{y},\omega)\,, \tag{2.28}$$

$\mathcal{S}_{\boldsymbol{v},i}$ is the scaling operator that accounts for the Doppler effect observed by the ith receiver due to a moving target with velocity $\boldsymbol{v}$ at location $\boldsymbol{y}$, and $\mathcal{G}_{\boldsymbol{y},i}$ is the operator that accounts for the wave propagation in the stationary background from the target to the ith receiver. Note that for a stationary target located at $\boldsymbol{y}$, the forward-propagation is comprised of only $\mathcal{G}_{\boldsymbol{y},i}$ [47].

$\mathcal{S}_{\boldsymbol{v},i}$ is given by

$$\mathcal{S}_{\boldsymbol{v},i}[u](\omega) = \int W_v(\boldsymbol{v}', \boldsymbol{v}) \mu_{\boldsymbol{y},\boldsymbol{v}',i}\, u(\boldsymbol{y}, \boldsymbol{v}', \mu_{\boldsymbol{y},\boldsymbol{v}',i}\, \omega) d\boldsymbol{v}', \tag{2.29}$$

where $W_v(\boldsymbol{v}', \boldsymbol{v})$ is a windowing function of unit amplitude in the velocity space centered at the hypothetical velocity $\boldsymbol{v}$. For notational simplicity, we write $\mu_{\boldsymbol{y},\boldsymbol{v},i} := \mu_{\boldsymbol{y},\boldsymbol{v},\mathbf{x}_i}$.

We define $\mathcal{G}_{\boldsymbol{y},i}$ in (2.27) as

$$\begin{aligned} \mathcal{G}_{\boldsymbol{y},i}[u](\omega) &= \int W_s(\boldsymbol{y}', \boldsymbol{y}) \hat{g}(\mathbf{x}_i, \boldsymbol{y}', \omega) u(\boldsymbol{y}', \boldsymbol{v}, \omega) d\boldsymbol{y}' \\ &= \int_{D_W(\boldsymbol{y})} \hat{g}(\mathbf{x}_i, \boldsymbol{y}', \omega) u(\boldsymbol{y}', \boldsymbol{v}, \omega) d\boldsymbol{y}'. \end{aligned} \tag{2.30}$$

In (2.30), $W_s(\boldsymbol{y}', \boldsymbol{y})$ is a spatial windowing function of unit amplitude centered at a hypothetical target location $\boldsymbol{y}$ at time $t = 0$, and $\hat{g}(\mathbf{x}_i, \boldsymbol{y}', \omega)$ is given by (2.21).

We define the back-propagation operator as the inverse of $\mathcal{P}_{\boldsymbol{y},\boldsymbol{v},i}$ and denote it with $\mathcal{P}^{-1}_{\boldsymbol{y},\boldsymbol{v},i}$. Using (2.27), $\mathcal{P}^{-1}_{\boldsymbol{y},\boldsymbol{v},i}$ can be expressed as

$$\mathcal{P}^{-1}_{\boldsymbol{y},\boldsymbol{v},i} = \mathcal{S}^{-1}_{\boldsymbol{v},i} \mathcal{G}^{-1}_{\boldsymbol{y},i}, \tag{2.31}$$

where $\mathcal{G}^{-1}_{\boldsymbol{y},i}$ is the inverse of $\mathcal{G}_{\boldsymbol{y},i}$, and $\mathcal{S}^{-1}_{\boldsymbol{v},i}$ is the inverse of $\mathcal{S}_{\boldsymbol{v},i}$. Note that if $\mathcal{P}^{-1}$ does not exist, we replace it with a suitable pseudoinverse of $\mathcal{P}$.

Let $\hat{m}_i$ denote the measurement at the ith receiver, and let there be a target centered at $(\boldsymbol{y}, \boldsymbol{v})$ in the position and velocity spaces. We can now express the measurement, $\hat{m}_i$, at the ith receiver in terms of the measurement, $\hat{m}_j$, at the jth receiver by back-propagating $\hat{m}_j$ measured at $\mathbf{x}_j$ to $(\boldsymbol{y}, \boldsymbol{v})$ in the position and velocity spaces via the back-propagation operator and then forward-propagating the resulting field to $\mathbf{x}_i$ via the forward-propagation operator. Thus, in an ideal scenario where there is no additive noise in the scattered field measurements, we obtain the following passive measurement model that relates the scattered field measurements $\hat{m}_i$ and $\hat{m}_j$:

$$\hat{m}_i(\omega) = \mathcal{P}_{\boldsymbol{y},\boldsymbol{v},i} \mathcal{P}^{-1}_{\boldsymbol{y},\boldsymbol{v},j} \hat{m}_j(\omega). \tag{2.32}$$

Figure 2 illustrates the back-propagation of the scattered field measurements at the jth receiver to a hypothetical target position and a hypothetical target velocity by the operator $\mathcal{P}^{-1}_{\boldsymbol{y},\boldsymbol{v},j}$ and forward-propagation of the resulting field to the ith receiver via the operator $\mathcal{P}_{\boldsymbol{y},\boldsymbol{v},i}$. For clarity, we factored the back- and forward-propagation operator into two parts—the operator associated with the background wave propagation, $\mathcal{G}$, as shown in Figure 2(a), and the operator associated with the Doppler scaling due to the movement of target, as shown

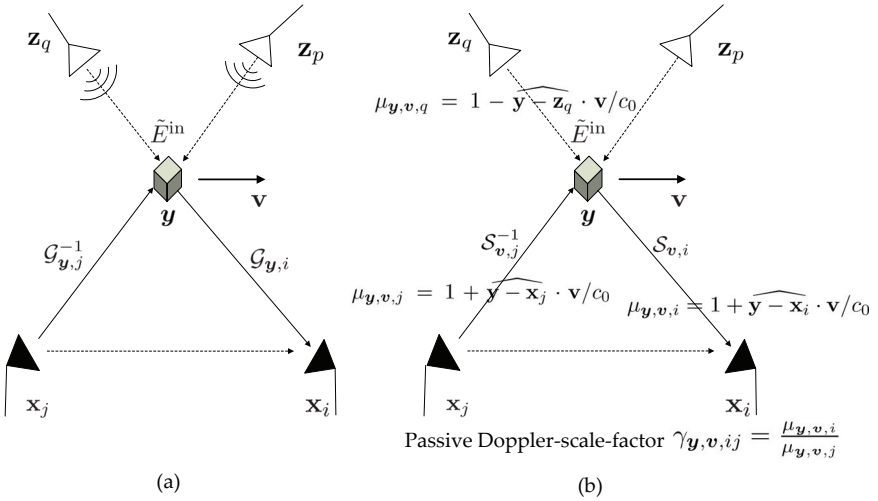

$$\mathcal{P}_{\boldsymbol{y},\boldsymbol{v},i} = \mathcal{G}_{\boldsymbol{y},i}\mathcal{S}_{\boldsymbol{v},i}$$

Figure 2. (a) *An illustration of the operator $\mathcal{G}$ and its inverse.* (b) *An illustration of the operator $\mathcal{S}$ and its inverse. The Doppler scaling effect observed by the jth receiver is removed via $\mathcal{S}_{\boldsymbol{v},j}$ for a hypothetical velocity. The Doppler scaling effect on the incident waveform observed by the ith receiver is then incorporated via $\mathcal{S}_{\boldsymbol{v},i}$. The measurement at $\mathbf{x}_j$ is mapped back to a hypothetical target location via $\mathcal{P}^{-1}_{\boldsymbol{y},\boldsymbol{v},j} = \mathcal{S}^{-1}_{\boldsymbol{v},j}\mathcal{G}^{-1}_{\boldsymbol{y},j}$. After the inverse scaling and scaling operations, the resulting field is mapped to $\mathbf{x}_i$ via $\mathcal{P}_{\boldsymbol{y},\boldsymbol{v},i} = \mathcal{G}_{\boldsymbol{y},i}\mathcal{S}_{\boldsymbol{v},i}$.*

in Figure 2(b). Note that in the presence of noise, when $\hat{m}_j$ is back-propagated, not only the noise-free measurement, $\hat{m}^{(0)}_j$, but also the noise at the jth receiver, $\hat{n}_j$, is back-propagated. Thus, the full expression for the passive measurement model becomes

$$\begin{aligned}\hat{m}_i(\omega) &= \mathcal{P}_{\boldsymbol{y},\boldsymbol{v},i}\mathcal{P}^{-1}_{\boldsymbol{y},\boldsymbol{v},j}\hat{m}^{(0)}_j(\omega) + \mathcal{P}_{\boldsymbol{y},\boldsymbol{v},i}\mathcal{P}^{-1}_{\boldsymbol{y},\boldsymbol{v},j}\hat{n}_j(\omega) + \hat{n}_i(\omega)\\ &= \mathcal{P}_{\boldsymbol{y},\boldsymbol{v},i}\mathcal{P}^{-1}_{\boldsymbol{y},\boldsymbol{v},j}\hat{m}_j(\omega) + \hat{n}_i(\omega).\end{aligned} \tag{2.33}$$

In many applications, the moving target model can be simplified to a point scatterer moving at a constant velocity, i.e.,

$$q_{\boldsymbol{v}}(\boldsymbol{y}) = \rho\,\delta(\boldsymbol{y}-\boldsymbol{y}_0)\delta(\boldsymbol{v}-\boldsymbol{v}_0), \tag{2.34}$$

where ρ is the reflectivity of the point target located at $\boldsymbol{y}_0$, at time $t = 0$, moving with velocity $\boldsymbol{v}_0$. Thus, for a point target moving at a constant velocity, the forward-propagation operator in (2.27) reduces to

$$\mathcal{P}_{\boldsymbol{y}_0,\boldsymbol{v}_0,i}[u](\omega) = \hat{g}(\mathbf{x}_i,\boldsymbol{y}_0,\omega)\mu_{\boldsymbol{y}_0,\boldsymbol{v}_0,i}u(\mu_{\boldsymbol{y}_0,\boldsymbol{v}_0,i}\,\omega), \tag{2.35}$$

where $\hat{g}(\mathbf{x}_i,\boldsymbol{y}_0,\omega)$ is given by (2.21) and $\mu_{\boldsymbol{y}_0,\boldsymbol{v}_0,i}$ is given by (2.17). Accordingly, the back-propagation operator in (2.31) becomes

$$\mathcal{P}^{-1}_{\boldsymbol{y}_0,\boldsymbol{v}_0,i}[\hat{m}_i](\omega) = \frac{1}{\mu_{\boldsymbol{y}_0,\boldsymbol{v}_0,i}}\hat{m}_i\left(\frac{\omega}{\mu_{\boldsymbol{y}_0,\boldsymbol{v}_0,i}}\right)\frac{1}{\hat{g}\left(\mathbf{x}_i,\boldsymbol{y}_0,\frac{\omega}{\mu_{\boldsymbol{y}_0,\boldsymbol{v}_0,i}}\right)}. \tag{2.36}$$

Using (2.35) and (2.36), for a moving point target, (2.33) becomes

$$\begin{aligned}\hat{m}_i(\omega) &= \mathcal{P}_{\boldsymbol{y}_0,\boldsymbol{v}_0,i}\mathcal{P}^{-1}_{\boldsymbol{y}_0,\boldsymbol{v}_0,j}\hat{m}_j(\omega) + \hat{n}_i(\omega) \\ &= \gamma_{\boldsymbol{y}_0,\boldsymbol{v}_0,ij}\,\hat{m}_j(\gamma_{\boldsymbol{y}_0,\boldsymbol{v}_0,ij}\omega)\frac{\hat{g}(\mathbf{x}_i,\boldsymbol{y}_0,\omega)}{\hat{g}(\mathbf{x}_j,\boldsymbol{y}_0,\gamma_{\boldsymbol{y}_0,\boldsymbol{v}_0,ij}\,\omega)} + \hat{n}_i(\omega),\end{aligned} \tag{2.37}$$

where $\gamma_{\boldsymbol{y},\boldsymbol{v},ij}$ is the ratio of the Doppler-scale-factors with respect to the ith and jth receivers given by

$$\gamma_{\boldsymbol{y}_0,\boldsymbol{v}_0,ij} := \frac{\mu_{\boldsymbol{y}_0,\boldsymbol{v}_0,i}}{\mu_{\boldsymbol{y}_0,\boldsymbol{v}_0,j}} = \frac{1+\widehat{\mathbf{y}_0-\mathbf{x}_i}\cdot\mathbf{v}_0/c_0}{1+\widehat{\mathbf{y}_0-\mathbf{x}_j}\cdot\mathbf{v}_0/c_0} \tag{2.38}$$

with $\mathbf{y}_0 = (\boldsymbol{y}_0, h(\boldsymbol{y}_0))$ and $\mathbf{v}_0 = (\boldsymbol{v}_0, Dh(\boldsymbol{y}_0)\cdot\boldsymbol{v}_0)$. Note that $\gamma_{\boldsymbol{y},\boldsymbol{v},ij}$ is the *Doppler-hitchhiker-scale-factor* defined in [52]. Due to the static nature of the receivers in the present work, we refer to $\gamma_{\boldsymbol{y},\boldsymbol{v},ij}$ as the *passive-Doppler-scale-factor*.

Substituting (2.21) into (2.37), we obtain

$$\hat{m}_i(\omega) = \frac{|\mathbf{y}_0-\mathbf{x}_j|}{|\mathbf{y}_0-\mathbf{x}_i|}\gamma_{\boldsymbol{y}_0,\boldsymbol{v}_0,ij}\mathrm{e}^{-\mathrm{i}k\,(|\mathbf{y}_0-\mathbf{x}_i|-\gamma_{\boldsymbol{y}_0,\boldsymbol{v}_0,ij}|\mathbf{y}_0-\mathbf{x}_j|)}\hat{m}_j(\gamma_{\boldsymbol{y}_0,\boldsymbol{v}_0,ij}\,\omega) + \hat{n}_i(\omega), \tag{2.39}$$

where $k = \omega/c_0$.

For N receivers located at $\mathbf{x}_1,\ldots,\mathbf{x}_N$, a vector measurement model can be formed by taking one of the receivers as a reference. Without loss of generality, we take the jth receiver as a reference and form the following measurement vector:

$$\mathbf{m} = \begin{bmatrix}\hat{m}_1 & \hat{m}_2 & \cdots & \hat{m}_N\end{bmatrix}^T. \tag{2.40}$$

Similarly, we can vectorize the "reference measurements" and the noise as follows:

$$\mathbf{m_r} = \begin{bmatrix}\hat{m}_j & \hat{m}_j & \cdots & \hat{m}_j\end{bmatrix}^T, \tag{2.41}$$

$$\mathbf{n} = \begin{bmatrix}\hat{n}_1 & \hat{n}_2 & \cdots & \hat{n}_N\end{bmatrix}^T, \tag{2.42}$$

where $\hat{n}_i$, $i \neq j$, is the additive thermal noise at the ith receiver. Note that $\mathbf{m}, \mathbf{m_r}$, and $\mathbf{n}$ are all $(N-1)$-dimensional vectors.

The composition of the back-propagation and forward-propagation operators can be represented as a diagonal matrix given by

$$\mathbf{P}_{\boldsymbol{y},\boldsymbol{v}} = \mathrm{diag}\begin{bmatrix}\mathcal{P}_{\boldsymbol{y},\boldsymbol{v},1}\mathcal{P}^{-1}_{\boldsymbol{y},\boldsymbol{v},j} & \mathcal{P}_{\boldsymbol{y},\boldsymbol{v},2}\mathcal{P}^{-1}_{\boldsymbol{y},\boldsymbol{v},j} & \cdots & \mathcal{P}_{\boldsymbol{y},\boldsymbol{v},N}\mathcal{P}^{-1}_{\boldsymbol{y},\boldsymbol{v},j}\end{bmatrix}, \tag{2.43}$$

where $i \neq j$ and $\mathbf{P}_{\boldsymbol{y},\boldsymbol{v}}$ is $(N-1)\times(N-1)$.

Using (2.33), (2.40)–(2.43), we form a vectorized passive measurement model as follows:

$$\mathbf{m}(\omega) = \mathbf{P}_{\boldsymbol{y},\boldsymbol{v}}\mathbf{m_r}(\omega) + \mathbf{n}(\omega) \tag{2.44}$$

for some range of ω. Note that in (2.44), all operations are understood to be elementwise.

The measurement model in (2.44) can be extended by taking each one of the N measurements as a reference which will result in measurement, reference measurement, and noise vectors of length $N(N-1)$. However, to simplify our notation and without loss of generality, we assume only one of the measurements as a reference.

3. Imaging of moving targets as a test of position- and velocity-resolved binary hypothesis. We formulate the imaging problem as a binary hypothesis testing problem using the passive moving target imaging model introduced in section 2.2. The binary hypothesis based approach has its roots in the GLRT [31, 32]. This approach provides a particularly suitable framework for the sparse aperture arrays due to the limited data available. In this formalism, we extract a position- and velocity-resolved test-statistic. The image is then formed in the $(\boldsymbol{y}, \boldsymbol{v})$ domain with the position- and velocity-resolved test-statistic where the location, possibly the shapes of the targets, and their velocities can be identified by thresholding the resulting four-dimensional test-statistic image.

In this section, we first set up a position- and velocity-resolved binary hypothesis test and next determine a test-statistic for each location $(\boldsymbol{y}, h(\boldsymbol{y})) \in \mathbb{R}^3$ and each velocity $(\boldsymbol{v}, Dh(\boldsymbol{y}) \cdot \boldsymbol{v}) \in \mathbb{R}^3$ in the position and velocity spaces using the passive measurement model for moving targets developed in section 2.2. We determine a test-statistic by maximizing the SNR of the test-statistic while constraining the associated discriminant functional to be linear.

The passive moving target imaging problem can be formulated as a test of the following position- and velocity-resolved binary hypotheses:

$$\begin{aligned} \mathcal{H}_0 :&\quad \mathbf{m} = \mathbf{n}, \\ \mathcal{H}_1 :&\quad \mathbf{m} = \mathbf{P}_{\boldsymbol{y},\boldsymbol{v}} \mathbf{m}_{\mathbf{r}} + \mathbf{n}, \end{aligned} \tag{3.1}$$

where $\mathbf{P}_{\boldsymbol{y},\boldsymbol{v}}, \mathbf{m}_{\mathbf{r}}, \mathbf{m}$, and $\mathbf{n}$ are as defined in (2.40)–(2.44).

The null hypothesis states that the measurement is due to noise, whereas the alternative hypothesis states that the measurement is due to a target located at $\boldsymbol{y}$ moving with velocity $\boldsymbol{v}$.

To design a discriminant functional, we first determine the first- and second-order statistics of the random processes involved under the two hypotheses.

Let $\mathbf{R}_{\mathbf{n}}$ be the autocovariance of the noise vector $\mathbf{n}$, i.e.,

$$\mathbf{R}_{\mathbf{n}}(\omega, \omega') = \mathrm{E}\left[\mathbf{n}(\omega)\mathbf{n}^H(\omega')\right], \tag{3.2}$$

and let $\mathbf{R}_{\mathbf{n}_{\mathbf{r}}}$ be the autocovariance of the noise vector $\mathbf{n}_{\mathbf{r}} := [\hat{n}_j, \hat{n}_j, \ldots, \hat{n}_j]$, i.e.,

$$\mathbf{R}_{\mathbf{n}_{\mathbf{r}}}(\omega, \omega') = \mathrm{E}\left[\mathbf{n}_{\mathbf{r}}(\omega)\mathbf{n}_{\mathbf{r}}^H(\omega')\right]. \tag{3.3}$$

Then, using (2.33), (2.41), (2.42), (3.1), (3.2), and (3.3), we obtain

$$\mathrm{E}\left[\mathbf{m}|\mathcal{H}_0\right] = \mathbf{0}, \tag{3.4}$$

$$\mathrm{Cov}\left[\mathbf{m}|\mathcal{H}_0\right] = \mathbf{R}_{\mathbf{n}} =: \mathbf{R}_0, \tag{3.5}$$

$$\mathrm{E}\left[\mathbf{m}|\mathcal{H}_1\right] = \mathbf{P}_{\boldsymbol{y},\boldsymbol{v}}\mathrm{E}\left[\mathbf{m}_{\mathbf{r}}|\mathcal{H}_1\right] = \mathbf{P}_{\boldsymbol{y},\boldsymbol{v}}\overline{\mathbf{m}}_{\mathbf{r}}, \tag{3.6}$$

$$\mathrm{Cov}\left[\mathbf{m}|\mathcal{H}_1\right] = \mathbf{P}_{\boldsymbol{y},\boldsymbol{v}}\mathbf{R}_{\mathbf{n}_{\mathbf{r}}}\mathbf{P}_{\boldsymbol{y},\boldsymbol{v}}^H + \mathbf{R}_{\mathbf{n}} =: \mathbf{R}_1, \tag{3.7}$$

where E denotes the expectation operator, Cov denotes the covariance operator, $\overline{\mathbf{m}}_{\mathbf{r}}$ denotes $\mathrm{E}\left[\mathbf{m}_{\mathbf{r}}|\mathcal{H}_1\right]$, and $\mathbf{P}_{\boldsymbol{y},\boldsymbol{v}}^H$ denotes the Hermitian transpose of $\mathbf{P}_{\boldsymbol{y},\boldsymbol{v}}$.

The linear discriminant functional involved in our problem has the form

$$\lambda = \langle \mathbf{m}, \mathbf{w} \rangle := \int \mathbf{w}^H \mathbf{m} d\omega = \sum_{i, i \neq j} \int w_i^*(\omega)\hat{m}_i(\omega) d\omega, \tag{3.8}$$

where λ denotes the the output of the discriminant functional, which we call the *test-statistic*, and $\mathbf{w}$ is a template given by

$$\mathbf{w} = \begin{bmatrix} w_1 & w_2 & \cdots & w_N \end{bmatrix}^T. \tag{3.9}$$

Equation (3.8) is a general form for a linear discriminant functional and can be applied to both single and multiple frequency measurements. For single frequency measurements, the integral can simply be omitted.

We determine the template by maximizing the SNR of λ. The expression for the SNR of λ for processes with finite first- and second-order statistics is given as [33]

$$\mathrm{SNR}_\lambda = \frac{|\mathrm{E}[\lambda|\mathcal{H}_1] - \mathrm{E}[\lambda|\mathcal{H}_0]|}{\sqrt{1/2(\mathrm{Var}[\lambda|\mathcal{H}_1] + \mathrm{Var}[\lambda|\mathcal{H}_0])}}. \tag{3.10}$$

Each term in (3.10) can be determined using (3.4)–(3.7). The numerator is given by

$$\mathrm{E}[\lambda|\mathcal{H}_1] - \mathrm{E}[\lambda|\mathcal{H}_0] = \langle \mathbf{P}_{\boldsymbol{y},\boldsymbol{v}}\overline{\mathbf{m}}_\mathbf{r}, \mathbf{w}\rangle. \tag{3.11}$$

The variance of λ can be expressed as

$$\mathrm{Var}[\lambda|\mathcal{H}_\ell] = \mathrm{E}\left[|\langle \mathbf{m}, \mathbf{w}\rangle|^2|\mathcal{H}_\ell\right], \quad \ell = 0, 1, \tag{3.12}$$

$$= \int \mathbf{w}^H \mathbf{R}_\ell \mathbf{w} d\omega d\omega' \tag{3.13}$$

$$=: \langle \mathcal{R}_\ell \mathbf{w}, \mathbf{w}\rangle, \quad \ell = 0, 1, \tag{3.14}$$

where $\mathcal{R}_\ell$, $\ell = 0, 1$, is a symmetric nonnegative definite integral operator with the matrix kernel $\mathbf{R}_\ell$. Note that the integration in (3.12) should be understood to be elementwise. Plugging (3.12) into (3.10), we obtain

$$\mathrm{Var}[\lambda|\mathcal{H}_1] + \mathrm{Var}[\lambda|\mathcal{H}_0] = \int \mathbf{w}^H [\mathbf{R}_1 + \mathbf{R}_0] \mathbf{w} d\omega d\omega' \tag{3.15}$$

$$= \int \mathbf{w}^H \underbrace{\left[\mathbf{P}_{\boldsymbol{y},\boldsymbol{v}}\mathbf{R}_{\mathbf{n}_\mathbf{r}}\mathbf{P}_{\boldsymbol{y},\boldsymbol{v}}^H + 2\mathbf{R}_\mathbf{n}\right]}_{2\overline{\mathbf{R}}} \mathbf{w} d\omega d\omega' \tag{3.16}$$

$$=: \left\langle 2\overline{\mathcal{R}}\mathbf{w}, \mathbf{w}\right\rangle, \tag{3.17}$$

where $\overline{\mathcal{R}}$ is a symmetric, nonnegative definite operator with the matrix kernel $\overline{\mathbf{R}}$.

Using (3.10), (3.11), and (3.15), SNR_λ^2 can be expressed in terms of the unknown template as follows:

$$J(\mathbf{w}) = \mathrm{SNR}_\lambda^2 = \frac{|\langle \mathbf{P}_{\boldsymbol{y},\boldsymbol{v}}\overline{\mathbf{m}}_\mathbf{r}, \mathbf{w}\rangle|^2}{1/2\left\langle (\mathcal{R}_1 + \mathcal{R}_0)\mathbf{w}, \mathbf{w}\right\rangle}. \tag{3.18}$$

The optimal linear template maximizing $J(\mathbf{w})$ is then

$$\mathbf{w}_{\mathrm{opt}} = \overline{\mathcal{R}}^{-1}\mathbf{P}_{\boldsymbol{y},\boldsymbol{v}}\overline{\mathbf{m}}_\mathbf{r}. \tag{3.19}$$

Equation (3.19) shows that the optimal template is position and velocity dependent. A detailed derivation of the optimal linear template can be found in Appendix A.

Under the assumption that the noise at different receivers is uncorrelated and wide-sense stationary, $\mathbf{R_n}$ reduces to a diagonal matrix. Without loss of generality, if the first receiver is the reference, then

$$R_n^{ii}(\omega,\omega') = S_n^{i+1}(\omega)\delta(\omega-\omega'), \qquad i=1,\dots,N-1, \tag{3.20}$$

where $S_n^i(\omega)$ is the power spectral density function of the noise. Note that if each component of the noise vector is white, $S_n^i(\omega), i=1,\dots,N, i\neq j$, becomes constant.

We define

$$\overline{\mathbf{S}}(\omega) = \int \overline{\mathbf{R}}(\omega,\omega')d\omega'. \tag{3.21}$$

Thus, under the wide-sense stationarity assumption, (3.19) becomes

$$\mathbf{w}_{\text{opt}} = \overline{\mathbf{S}}^{-1}(\omega)\mathbf{P}_{\boldsymbol{y},\boldsymbol{v}}(\omega)\overline{\mathbf{m}}_{\mathbf{r}}(\omega), \tag{3.22}$$

where $\overline{\mathbf{S}}^{-1}$ is the inverse of $\overline{\mathbf{S}}$.

From (3.21) and (3.16), $\overline{\mathbf{S}}^{-1}$ can be approximated by a diagonal matrix (for a detailed derivation, see Appendix B).

We denote diagonal elements of $\overline{\mathbf{S}}^{-1}$ by $\overline{S}_i^{-1}(\omega), i=1,\dots,N$, and $i\neq j$, which is a function of $S_n^i(\omega)$ and the kernel of $\mathbf{P}_{\boldsymbol{y},\boldsymbol{v}}$.

For a moving point target located at $\boldsymbol{y}$, moving with a hypothetical velocity $\boldsymbol{v}$, each component of the optimal template becomes

$$w_i = \overline{S}_i^{-1}(\omega)\frac{|\mathbf{y}-\mathbf{x}_j|}{|\mathbf{y}-\mathbf{x}_i|}\gamma_{\boldsymbol{y},\boldsymbol{v},ij}\mathrm{e}^{-ik\left(|\mathbf{y}-\mathbf{x}_i|-\gamma_{\boldsymbol{y},\boldsymbol{v},ij}|\mathbf{y}-\mathbf{x}_j|\right)}\mathrm{E}\left[\hat{m}_j(\gamma_{\boldsymbol{y},\boldsymbol{v},ij}\,\omega)\right], \tag{3.23}$$

where $i=1,\dots,N$, and $i\neq j$, and $\gamma_{\boldsymbol{y},\boldsymbol{v},ij}$ is given by (2.38).

The first term in (3.23) is a prewhitening filter due to colored noise, the second term involves scaling due to geometrical spreading factors and the passive-Doppler-scale-factor, the third term involves delay due to the path difference between the two receivers and a temporal dilation due to the passive-Doppler-scale-factor, and the last term involves averaged dilated reference measurement.

Thus, the output of the linear discriminant functional can be viewed as a summation of the correlations between the filtered, delayed, scaled (or dilated) replica of the reference measurement m_j and the measurement $m_i, i\neq j$, which is given by

$$\lambda(\boldsymbol{y},\boldsymbol{v}) = \sum_{i\neq j}\int \frac{|\mathbf{y}-\mathbf{x}_j|}{|\mathbf{y}-\mathbf{x}_i|}\mathrm{E}\left[m_j'\left(\frac{t-|\mathbf{y}-\mathbf{x}_i|/c_0}{\gamma_{\boldsymbol{y},\boldsymbol{v},ij}}+\frac{|\mathbf{y}-\mathbf{x}_j|}{c_0}\right)\right]m_i^*(t)dt, \tag{3.24}$$

where $m_j'(t)$ is the filtered version of $m_j(t)$ with the filtering given by $\overline{S}_i^{-1}(\omega)$.

Note that for stationary targets, the passive-Doppler-scaling factor, $\gamma_{\boldsymbol{y},\boldsymbol{v},ij}$, becomes 1, and the test-statistic in (3.24) reduces to the one in passive imaging of stationary targets using distributed apertures in free space [47].

We use $\lambda(\boldsymbol{y},\boldsymbol{v})$ to form a four-dimensional image of the scene, which shows the distribution of the targets in the two-dimensional position space as well as their corresponding velocities in the two-dimensional velocity space. In the next section, we analyze the resolution of our passive moving target imaging method.

4. Resolution analysis. In this section, we assume that the surface topography is flat, i.e., $h(\boldsymbol{y}) = h$, for some $\boldsymbol{y} \in \mathbb{R}^2$ and set $\mathbf{y} = [\boldsymbol{y}, h]$, $\mathbf{v} = [\boldsymbol{v}, 0]$. We focus our analysis on the moving point target model given by (2.34) and analyze how it is resolved in the four-dimensional image $\lambda(\boldsymbol{y},\boldsymbol{v}), \boldsymbol{y},\boldsymbol{v} \in \mathbb{R}^2$.

We define the expected value of the image of a moving point target, represented by the Dirac-delta function in position and velocity spaces, as the point spread function (PSF), $K(\boldsymbol{y},\boldsymbol{y}_0;\boldsymbol{v},\boldsymbol{v}_0)$, of the four-dimensional imaging operator with $\boldsymbol{y}$ serving as the spatial index of the image, $\boldsymbol{y}_0$ as the location of the point target (at time $t = 0$), $\boldsymbol{v}$ as the velocity index of the image, and $\boldsymbol{v}_0$ as the velocity of the point target, i.e.,

$$\begin{aligned} K(\boldsymbol{y},\boldsymbol{y}_0;\boldsymbol{v},\boldsymbol{v}_0) &:= \mathrm{E}\left[\lambda(\boldsymbol{y},\boldsymbol{v})\right] \\ &= \langle \mathrm{E}\left[\mathbf{m}\right], \overline{\mathcal{R}}^{-1}\mathbf{P}_{\boldsymbol{y},\boldsymbol{v}}\overline{\mathbf{m}}_{\mathbf{r}}\rangle. \end{aligned} \tag{4.1}$$

Without loss of generality, we first assume that there is a single pair of receivers present and a single transmitter in the scene. This allows us to simplify our analysis and distill the important aspects of our analysis that can be readily generalized. We next extend our results to the case where there are multiple pairs of receivers and multiple transmitters.

4.1. Resolution analysis for two receivers and a single transmitter.

4.1.1. PSF of the imaging operator. The transmitter is assumed to be located at $\mathbf{z}_1$ transmitting waveform p_1 at time $t = -T_{\mathbf{z}_1}$. For a deterministic moving point target model given by (2.34), using (2.24), we have

$$\mathrm{E}\left[\hat{m}_j(\omega)\right] = \frac{-\omega^2\rho \mathrm{e}^{\mathrm{i}\phi_{\boldsymbol{y}_0,\boldsymbol{v}_0,\mathbf{x}_j,\mathbf{z}_1}}}{(4\pi)^2|\mathbf{y}_0-\mathbf{x}_j||\mathbf{y}_0-\mathbf{z}_1|\alpha^3_{\boldsymbol{y}_0,\boldsymbol{v}_0,\mathbf{x}_j,\mathbf{z}_1}}\hat{p}_1\left(\frac{\omega}{\alpha_{\boldsymbol{y}_0,\boldsymbol{v}_0,\mathbf{x}_j,\mathbf{z}_1}}\right), \tag{4.2}$$

where $\phi_{\boldsymbol{y}_0,\boldsymbol{v}_0,\mathbf{x}_j,\mathbf{z}_1}$ and $\alpha_{\boldsymbol{y}_0,\boldsymbol{v}_0,\mathbf{x}_j,\mathbf{z}_1}$ are as in (2.25) and (2.26), respectively.

We assume that there are two receivers located at $\mathbf{x}_1$ and $\mathbf{x}_2$ and take the measurement at $\mathbf{x}_1$ as the reference. Thus, from (3.8) and (3.23), we have

$$\begin{aligned} K(\boldsymbol{y},\boldsymbol{y}_0;\boldsymbol{v},\boldsymbol{v}_0) &= \mathrm{E}\left[\lambda(\boldsymbol{y},\boldsymbol{v})\right] \\ &= \frac{|\mathbf{y}-\mathbf{x}_1|}{|\mathbf{y}-\mathbf{x}_2|}\gamma_{\boldsymbol{y},\boldsymbol{v},21}\int \overline{S}_2^{-1}(\omega)\mathrm{e}^{-\mathrm{i}k\left(|\mathbf{y}-\mathbf{x}_2|-\gamma_{\boldsymbol{y},\boldsymbol{v},21}|\mathbf{y}-\mathbf{x}_1|\right)} \\ &\qquad \times \mathrm{E}\left[\hat{m}_1(\gamma_{\boldsymbol{y},\boldsymbol{v},21}\,\omega)\right]\mathrm{E}\left[\hat{m}_2^*(\omega)\right]d\omega, \end{aligned} \tag{4.3}$$

where $\gamma_{\boldsymbol{y},\boldsymbol{v},12}$ is given by (2.38) for $i = 2, j = 1$.

Using (4.2), (4.3) becomes

$$\begin{aligned} K(\boldsymbol{y},\boldsymbol{y}_0;\boldsymbol{v},\boldsymbol{v}_0) = \beta\int \overline{S}_2^{-1}(\omega)\omega^4\mathrm{e}^{-\mathrm{i}\,kr_{21}}\mathrm{e}^{\mathrm{i}k\left[\left(\frac{\gamma_{\boldsymbol{y},\boldsymbol{v},21}}{\alpha_{\boldsymbol{y}_0,\boldsymbol{v}_0,\mathbf{x}_1,\mathbf{z}_1}}-\frac{1}{\alpha_{\boldsymbol{y}_0,\boldsymbol{v}_0,\mathbf{x}_2,\mathbf{z}_1}}\right)\left(c_0T_{\mathbf{z}_1}-|\mathbf{y}_0-\mathbf{z}_1|\right)\right]} \\ \times\hat{p}_1\left(\frac{\gamma_{\boldsymbol{y},\boldsymbol{v},21}}{\alpha_{\boldsymbol{y}_0,\boldsymbol{v}_0,\mathbf{x}_1,\mathbf{z}_1}}\omega\right)\hat{p}_1^*\left(\frac{\omega}{\alpha_{\boldsymbol{y}_0,\boldsymbol{v}_0,\mathbf{x}_2,\mathbf{z}_1}}\right)d\omega, \end{aligned} \tag{4.4}$$

where

$$\beta = \frac{\rho^2|\mathbf{y}-\mathbf{x}_1|}{(4\pi)^4|\mathbf{y}_0-\mathbf{z}_1|^2|\mathbf{y}_0-\mathbf{x}_1||\mathbf{y}_0-\mathbf{x}_2||\mathbf{y}-\mathbf{x}_2|}\cdot\frac{\gamma^3_{\boldsymbol{y},\boldsymbol{v},21}}{\alpha^3_{\boldsymbol{y}_0,\boldsymbol{v}_0,\mathbf{x}_1,\mathbf{z}_1}\alpha^3_{\boldsymbol{y}_0,\boldsymbol{v}_0,\mathbf{x}_2,\mathbf{z}_1}} \tag{4.5}$$

and

$$r_{21} = |\mathbf{y}-\mathbf{x}_2| - \gamma_{\boldsymbol{y},\boldsymbol{v},21}|\mathbf{y}-\mathbf{x}_1| - (|\mathbf{y}_0-\mathbf{x}_2| - \gamma_{\boldsymbol{y},\boldsymbol{v},21}|\mathbf{y}_0-\mathbf{x}_1|)\,. \tag{4.6}$$

Note that if $T_{\mathbf{z}_1}$ is chosen to be equal to $|\mathbf{y}_0-\mathbf{z}_1|/c_0$, the second exponential term in (4.4) disappears.

Examining (4.4), we see that if

$$\frac{\gamma_{\boldsymbol{y},\boldsymbol{v},21}}{\alpha_{\boldsymbol{y}_0,\boldsymbol{v}_0,\mathbf{x}_1,\mathbf{z}_1}} = \frac{1}{\alpha_{\boldsymbol{y}_0,\boldsymbol{v}_0,\mathbf{x}_2,\mathbf{z}_1}}\,, \tag{4.7}$$

then (4.4) becomes

$$\begin{aligned} K(\boldsymbol{y},\boldsymbol{y}_0;\boldsymbol{v},\boldsymbol{v}_0) &= \frac{T^2|\mathbf{y}-\mathbf{x}_1|}{(4\pi)^4|\mathbf{y}_0-\mathbf{z}_1|^2|\mathbf{y}_0-\mathbf{x}_1||\mathbf{y}-\mathbf{x}_2|\alpha^6_{\boldsymbol{y}_0,\boldsymbol{v}_0,\mathbf{x}_2,\mathbf{z}_1}} \\ &\quad\times\int \overline{S}_2^{-1}(\omega)\omega^4 \mathrm{e}^{-\mathrm{i}\,kr_{21}}\left|\hat{p}_1\left(\frac{\omega}{\alpha_{\boldsymbol{y}_0,\boldsymbol{v}_0,\mathbf{x}_2,\mathbf{z}_1}}\right)\right|^2 d\omega, \end{aligned} \tag{4.8}$$

which defines the correlation of $|\overline{S}_2^{-1/2}(\omega)\omega^2\hat{p}_1(\frac{\omega}{\alpha_{\boldsymbol{y}_0,\boldsymbol{v}_0,\mathbf{x}_2,\mathbf{z}_1}})|$ with itself in time domain. Clearly, this correlation peaks when $r_{21}=0$, i.e.,

$$|\mathbf{y}-\mathbf{x}_2| - \gamma_{\boldsymbol{y},\boldsymbol{v},21}|\mathbf{y}-\mathbf{x}_1| = |\mathbf{y}_0-\mathbf{x}_2| - \gamma_{\boldsymbol{y},\boldsymbol{v},21}|\mathbf{y}_0-\mathbf{x}_1|\,. \tag{4.9}$$

Note that (4.8) can be interpreted as a generalized autoambiguity function of the transmitted waveform p_1 [44], which is a filtered and scaled version of the classical autoambiguity function.

The analysis above shows that the PSF of the imaging operator for two receivers and one transmitter reaches its maximum when the two conditions given in (4.7) and (4.9) are satisfied.

4.1.2. Passive iso-Doppler and iso-range manifolds in position and velocity spaces. Using (4.7) and (2.26), we have

$$\gamma_{\boldsymbol{y},\boldsymbol{v},21} = \frac{\alpha_{\boldsymbol{y}_0,\boldsymbol{v}_0,\mathbf{x}_1,\mathbf{z}_1}}{\alpha_{\boldsymbol{y}_0,\boldsymbol{v}_0,\mathbf{x}_2,\mathbf{z}_1}} = \frac{1+\widehat{\mathbf{y}_0-\mathbf{x}_2}\cdot\mathbf{v}_0/c_0}{1+\widehat{\mathbf{y}_0-\mathbf{x}_1}\cdot\mathbf{v}_0/c_0} = \gamma_{\boldsymbol{y}_0,\boldsymbol{v}_0,21}. \tag{4.10}$$

Since, in the slow-mover case, the speed of the target is much slower than the speed of light c_0, $\gamma_{\boldsymbol{y},\boldsymbol{v},21}$ can be approximated as follows:

$$\begin{aligned} \gamma_{\boldsymbol{y},\boldsymbol{v},21} &= 1+\frac{\widehat{\mathbf{y}-\mathbf{x}_2}\cdot\mathbf{v}/c_0 - \widehat{\mathbf{y}-\mathbf{x}_1}\cdot\mathbf{v}/c_0}{1+\widehat{\mathbf{y}-\mathbf{x}_1}\cdot\mathbf{v}/c_0} \\ &\approx 1+(\widehat{\mathbf{y}-\mathbf{x}_2}-\widehat{\mathbf{y}-\mathbf{x}_1})\cdot\mathbf{v}/c_0\,. \end{aligned} \tag{4.11}$$

Let

$$F_{21}(C) = \{(\boldsymbol{y}, \boldsymbol{v}) \in \mathbb{R}^2 \times \mathbb{R}^2 : \gamma_{\boldsymbol{y},\boldsymbol{v},21} = C\} \tag{4.12}$$

for some constant $C \in \mathbb{R}^+$. Using (4.11), $\gamma_{\boldsymbol{y},\boldsymbol{v},21} = C$ can be written as

$$(\widehat{\mathbf{y} - \mathbf{x}_2} - \widehat{\mathbf{y} - \mathbf{x}_1}) \cdot \mathbf{v} = (C-1)c_0. \tag{4.13}$$

Multiplying both sides of (4.13) by ω, we have

$$\frac{\omega}{c_0}(\widehat{\mathbf{y} - \mathbf{x}_2} - \widehat{\mathbf{y} - \mathbf{x}_1}) \cdot \mathbf{v} = (C-1)\omega\,. \tag{4.14}$$

The left-hand side of (4.14) is the *hitchhiker-Doppler* defined in [53]. Furthermore, for a fixed frequency, ω_0, (4.14) becomes the *DSAH-Doppler* defined in [52]. In this regard, we refer to the manifold defined by (4.12) as the *passive-iso-Doppler manifold*. Thus, (4.10) specifies a passive-iso-Doppler manifold with respect to two receivers located at $\mathbf{x}_1$ and $\mathbf{x}_2$. The test-statistic due to a moving point target located at $\boldsymbol{y}_0$ moving with velocity $\boldsymbol{v}_0$ is constant on this manifold.

Substituting (4.10) into the right-hand side of (4.9), we obtain

$$|\mathbf{y} - \mathbf{x}_2| - \gamma_{\boldsymbol{y},\boldsymbol{v},21}|\mathbf{y} - \mathbf{x}_1| = |\mathbf{y}_0 - \mathbf{x}_2| - \gamma_{\boldsymbol{y}_0,\boldsymbol{v}_0,21}|\mathbf{y}_0 - \mathbf{x}_1|. \tag{4.15}$$

Let

$$r_{21}(\boldsymbol{y}, \boldsymbol{v}) = |\mathbf{y} - \mathbf{x}_2| - \gamma_{\boldsymbol{y},\boldsymbol{v},21}|\mathbf{y} - \mathbf{x}_1|. \tag{4.16}$$

We refer to $r_{21}(\boldsymbol{y}, \boldsymbol{v})$ as the *passive-range* for a moving target with the passive Doppler-scale-factor $\gamma_{\boldsymbol{y},\boldsymbol{v},21}$. For a pair of receivers located at $\mathbf{x}_1$ and $\mathbf{x}_2$, let

$$R_{21}(C) = \{(\boldsymbol{y}, \boldsymbol{v}) \in \mathbb{R}^2 \times \mathbb{R}^2 : r_{21}(\boldsymbol{y}, \boldsymbol{v}) = C\}, \tag{4.17}$$

where $C \in \mathbb{R}^+$ is a constant. Equation (4.17) defines a manifold in the four-dimensional position and velocity space $(\boldsymbol{y}, \boldsymbol{v})$. We refer to the this manifold as the *passive-iso-range manifold*. Thus, (4.15) specifies a passive-iso-range manifold with respect to two receivers located at $\mathbf{x}_1$ and $\mathbf{x}_2$. The test-statistic due to a moving point target located at $\boldsymbol{y}_0$ moving with velocity $\boldsymbol{v}_0$ is constant on this manifold.

Based on the analysis above, we conclude that the PSF peaks at the intersection of the passive-iso-Doppler manifold defined by (4.10) and the passive-iso-range manifold defined by (4.15). The spreads along the passive-iso-Doppler manifold and the passive-iso-range manifold are both related to the shape of the generalized autoambiguity function defined by (4.8). Hence, the resolution of the reconstructed image in $(\boldsymbol{y}, \boldsymbol{v})$ is determined by the overlapping region between the passive-iso-Doppler and passive-iso-range manifolds. The cross-section of the overlapping region for a constant velocity determines the position resolution, while the cross-section of the overlapping region for a constant position determines the velocity resolution.

4.1.3. Two-dimensional passive iso-Doppler and iso-range contours. We consider the cross-sections of the passive-iso-Doppler and passive-iso-range manifolds for constant position and constant velocity in order to be able to visualize the four-dimensional PSF and to gain insight into the passive range and velocity resolutions.

Under the slow-mover assumption, (4.10) becomes

$$(\widehat{\mathbf{y}-\mathbf{x}_2}-\widehat{\mathbf{y}-\mathbf{x}_1})\cdot\boldsymbol{v}=(\widehat{\mathbf{y}_0-\mathbf{x}_2}-\widehat{\mathbf{y}_0-\mathbf{x}_1})\cdot\boldsymbol{v}_0. \tag{4.18}$$

We consider the two-dimensional cross-sections of the four-dimensional passive-iso-Doppler manifold defined by (4.10) for a constant velocity $\boldsymbol{v}_0$ and a constant position $\boldsymbol{y}_0$.

Using (4.18), we define

$$F_{\boldsymbol{v}_0,21}(C)=\{\boldsymbol{y}\in\mathbb{R}^2:(\widehat{\mathbf{y}-\mathbf{x}_2}-\widehat{\mathbf{y}-\mathbf{x}_1})\cdot\boldsymbol{v}_0=(\widehat{\mathbf{y}_0-\mathbf{x}_2}-\widehat{\mathbf{y}_0-\mathbf{x}_1})\cdot\boldsymbol{v}_0\} \tag{4.19}$$

and

$$F_{\boldsymbol{y}_0,21}(C)=\{\boldsymbol{v}\in\mathbb{R}^2:(\widehat{\mathbf{y}_0-\mathbf{x}_2}-\widehat{\mathbf{y}_0-\mathbf{x}_1})\cdot\boldsymbol{v}=(\widehat{\mathbf{y}_0-\mathbf{x}_2}-\widehat{\mathbf{y}_0-\mathbf{x}_1})\cdot\boldsymbol{v}_0\ \}. \tag{4.20}$$

For a pair of receivers located at $\mathbf{x}_1$ and $\mathbf{x}_2$ and target velocity $\boldsymbol{v}_0$, (4.19) specifies a passive-iso-Doppler curve in the two-dimensional position space. We refer to this curve as the *position-related passive-iso-Doppler contour*. Similarly, for a pair of receivers located at $\mathbf{x}_1$ and $\mathbf{x}_2$ and a target located at $\boldsymbol{y}_0$, (4.20) specifies a passive-iso-Doppler curve in the two-dimensional velocity space. We refer to this curve as the *velocity-related passive-iso-Doppler contour*.

Let ϕ_{12} be the angle between $\widehat{\mathbf{y}_0-\mathbf{x}_1}$ and $\widehat{\mathbf{y}_0-\mathbf{x}_2}$ and θ (θ_0) be the angle between $\boldsymbol{v}$ ($\boldsymbol{v}_0$) and $\widehat{\mathbf{y}_0-\mathbf{x}_2}-\widehat{\mathbf{y}_0-\mathbf{x}_1}$. Then, (4.20) can be expressed as

$$\begin{aligned}2\sin\left(\frac{\phi_{12}}{2}\right)|\boldsymbol{v}|\cos\theta&=2\sin\left(\frac{\phi_{12}}{2}\right)|\boldsymbol{v}_0|\cos\theta_0\\ \Rightarrow|\boldsymbol{v}|\cos\theta&=|\boldsymbol{v}_0|\cos\theta_0.\end{aligned} \tag{4.21}$$

Since $\{(|\boldsymbol{v}|,\theta)\in\mathbb{R}\times[0,2\pi]:|\boldsymbol{v}|\cos\theta=C\}$ for some constant C determines a straight line on the velocity plane, the velocity-related passive-iso-Doppler contour, specified by (4.20) and (4.21), corresponds to a line on the velocity plane that is perpendicular to the vector $\widehat{\mathbf{y}-\mathbf{x}_2}-\widehat{\mathbf{y}-\mathbf{x}_1}$ with its distance to the origin being $|\boldsymbol{v}|\cos\theta$.

Figures 3 and 4 illustrate the position-related passive-iso-Doppler and velocity-related passive-iso-Doppler contours, respectively. The scene is $[0,100]\times[0,100]\,\mathrm{m}^2$ with flat topography and discretized into 200×200 pixels. The range of the velocity is $[-20,20]\times[-20,20]\,\mathrm{m/s}$. The velocity plane is discretized into 400×400 pixels. The two receivers are located at $\mathbf{x}_1=[41.7\quad 0\quad 6]^T$ and $\mathbf{x}_2=[58.3\quad 0\quad 6]^T$, all in meters. The transmitter is located in the middle of the two receivers at $\mathbf{z}_0=[50\quad 0\quad 6]^T$ meters, and the point target is located at $\mathbf{y}_0=[60\quad 60\quad 0.1]^T$ meters, at time $t=0$, moving with velocity $[-10\quad 15\quad 0]\,\mathrm{m/s}$.

Similarly, we consider the cross-sections of the passive-iso-range manifold given in (4.15) for a constant velocity, $\boldsymbol{v}_0$, and a constant position, $\boldsymbol{y}_0$:

$$\begin{aligned}R_{\boldsymbol{v}_0,21}(C)=\{&\boldsymbol{y}\in\mathbb{R}^2:|\mathbf{y}-\mathbf{x}_2|-\gamma_{\boldsymbol{y},\boldsymbol{v}_0,21}|\mathbf{y}-\mathbf{x}_1|\\ &=|\mathbf{y}_0-\mathbf{x}_2|-\gamma_{\boldsymbol{y}_0,\boldsymbol{v}_0,21}|\mathbf{y}_0-\mathbf{x}_1|\}\end{aligned} \tag{4.22}$$

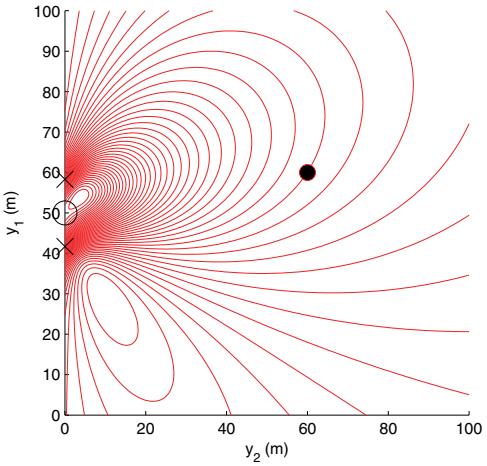

Figure 3. *Position-related passive-iso-Doppler contours associated with a single transmitter and two receivers in the two-dimensional position space. The blank circle shows the transmitter location, and the cross shows receiver locations. The solid circle shows the point target location.*

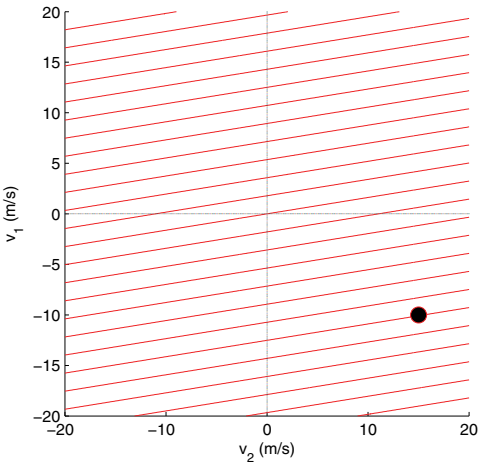

Figure 4. *Velocity-related passive-iso-Doppler contours associated with a single transmitter and two receivers in the two-dimensional velocity space. The solid circle shows the point target velocity.*

and

$$R_{\boldsymbol{y}_0,21}(C) = \{\boldsymbol{v} \in \mathbb{R}^2 : |\mathbf{y}_0 - \mathbf{x}_2| - \gamma_{\boldsymbol{y}_0,\boldsymbol{v},21}|\mathbf{y}_0 - \mathbf{x}_1| = |\mathbf{y}_0 - \mathbf{x}_2| - \gamma_{\boldsymbol{y}_0,\boldsymbol{v}_0,21}|\mathbf{y}_0 - \mathbf{x}_1|\}. \tag{4.23}$$

Note that under the slow-mover approximation given in (4.11), (4.23) reduces to (4.20). We refer to (4.22) as the *position-related passive-iso-range contour*. Figure 5 illustrates the position-related passive-iso-range contours. The settings of the scene, target, receivers, and transmitter are the same as those of Figure 3. Since under the slow-mover assumption $\gamma_{\boldsymbol{y},\boldsymbol{v},21}$ is close to

1, we see that the position-related passive-iso-range contours are similar to hyperbolas with foci at $\mathbf{x}_1$ and $\mathbf{x}_2$.

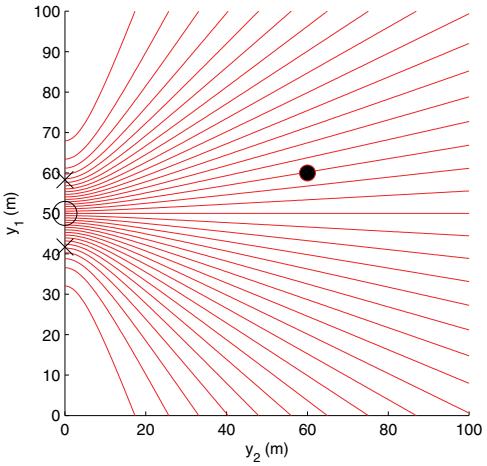

Figure 5. *Position-related passive-iso-range contours associated with a single transmitter and two receivers in two-dimensional position space. The blank circle shows the transmitter location, and the cross shows receiver locations. The solid circle shows the point target location.*

From the analysis in section 4.1 and the analysis above, we conclude that the velocity resolution is related to the spread of the velocity-related passive-iso-Doppler contours. The position resolution, on the other hand, can be related to the spread of the position-related passive-iso-Doppler contour or position-related passive-iso-range contour, depending on the Doppler and range ambiguities of the transmitted waveform: If the transmitted waveform has good Doppler resolution but poor range resolution, the position resolution primarily depends on the spread of the position-related passive-iso-Doppler contours. If, on the other hand, the transmitted waveform has only good range resolution, the position reconstruction primarily depends on the spread of the position-related passive-iso-range contours.

Note that if the transmitted waveform has both good Doppler and good range resolution, the position resolution depends on the cross-section of the intersection of the passive-iso-Doppler and passive-iso-range manifolds for constant velocity as described in section 4.1, which is neither the position-related passive-iso-Doppler contour nor the position-related passive-iso-range contour. However, this cross-section becomes one of the two types of contours described above as the range or Doppler resolution of the waveform degrades, or as the Doppler or range resolution improves.

4.2. Resolution analysis for multiple receivers and multiple transmitters. For multiple receivers ($N > 2$) and multiple transmitters located at $\mathbf{z}_q$, $q = 1, \ldots, M$ ($M > 1$), using (2.24),

(2.34), (3.8), and (3.23), we can show that the PSF of the imaging operator becomes

$$
\begin{aligned}
K(\boldsymbol{y},\boldsymbol{y}_0;\boldsymbol{v},\boldsymbol{v}_0) = \rho^2 \sum_{q=1}^{M}\sum_{i\neq j}^{N} C_1 \int \overline{S}_i^{-1}(\omega)\omega^4 \mathrm{e}^{-\mathrm{i}\,kr_{ij}} \\
\times \mathrm{e}^{\mathrm{i}k\left[\left(\frac{\gamma_{\boldsymbol{y},\boldsymbol{v},ij}}{\alpha_{\boldsymbol{y}_0,\boldsymbol{v}_0,\mathbf{x}_j,\mathbf{z}_q}}-\frac{1}{\alpha_{\boldsymbol{y}_0,\boldsymbol{v}_0,\mathbf{x}_i,\mathbf{z}_q}}\right)\left(cT_{\mathbf{z}_q}-|\mathbf{y}_0-\mathbf{z}_q|\right)\right]} \\
\times \hat{p}_q\left(\frac{\gamma_{\boldsymbol{y},\boldsymbol{v},ij}}{\alpha_{\boldsymbol{y}_0,\boldsymbol{v}_0,\mathbf{x}_j,\mathbf{z}_q}}\omega\right)\hat{p}_q^*\left(\frac{\omega}{\alpha_{\boldsymbol{y}_0,\boldsymbol{v}_0,\mathbf{x}_i,\mathbf{z}_q}}\right)d\omega \\
+\rho^2 \sum_{q\neq q'}^{M}\sum_{i\neq j}^{N} C_2 \int \overline{S}_i^{-1}(\omega)\omega^4 \mathrm{e}^{-\mathrm{i}\,kr_{ij}} \\
\times \mathrm{e}^{\mathrm{i}k\left[\frac{\gamma_{\boldsymbol{y},\boldsymbol{v},ij}}{\alpha_{\boldsymbol{y}_0,\boldsymbol{v}_0,\mathbf{x}_j,\mathbf{z}_q}}(c_0T_{\mathbf{z}_q}-|\mathbf{y}_0-\mathbf{z}_q|)-\frac{1}{\alpha_{\boldsymbol{y}_0,\boldsymbol{v}_0,\mathbf{x}_i,\mathbf{z}_{q'}}}(c_0T_{\mathbf{z}_{q'}}-|\mathbf{y}_0-\mathbf{z}_{q'}|)\right]} \\
\times \hat{p}_q\left(\frac{\gamma_{\boldsymbol{y},\boldsymbol{v},ij}}{\alpha_{\boldsymbol{y}_0,\boldsymbol{v}_0,\mathbf{x}_j,\mathbf{z}_q}}\omega\right)\hat{p}_{q'}^*\left(\frac{\omega}{\alpha_{\boldsymbol{y}_0,\boldsymbol{v}_0,\mathbf{x}_i,\mathbf{z}_{q'}}}\right)d\omega,
\end{aligned}
\tag{4.24}
$$

where

$$
\begin{aligned}
C_1 = \frac{|\mathbf{y}-\mathbf{x}_j|}{(4\pi)^4|\mathbf{y}_0-\mathbf{z}_q|^2|\mathbf{y}_0-\mathbf{x}_j||\mathbf{y}_0-\mathbf{x}_i||\mathbf{y}-\mathbf{x}_i|} \\
\times \frac{\gamma^3_{\boldsymbol{y},\boldsymbol{v},ij}}{\alpha^3_{\boldsymbol{y}_0,\boldsymbol{v}_0,\mathbf{x}_j,\mathbf{z}_q}\alpha^3_{\boldsymbol{y}_0,\boldsymbol{v}_0,\mathbf{x}_i,\mathbf{z}_q}},
\end{aligned}
\tag{4.25}
$$

$$
\begin{aligned}
C_2 = \frac{|\mathbf{y}-\mathbf{x}_j|}{(4\pi)^4|\mathbf{y}_0-\mathbf{z}_q||\mathbf{y}_0-\mathbf{z}_{q'}||\mathbf{y}_0-\mathbf{x}_j||\mathbf{y}_0-\mathbf{x}_i||\mathbf{y}-\mathbf{x}_i|} \\
\times \frac{\gamma^3_{\boldsymbol{y},\boldsymbol{v},ij}}{\alpha^3_{\boldsymbol{y}_0,\boldsymbol{v}_0,\mathbf{x}_j,\mathbf{z}_q}\alpha^3_{\boldsymbol{y}_0,\boldsymbol{v}_0,\mathbf{x}_i,\mathbf{z}_{q'}}},
\end{aligned}
\tag{4.26}
$$

and

$$
r_{ij} = |\mathbf{y}-\mathbf{x}_i| - \gamma_{\boldsymbol{y},\boldsymbol{v},ij}|\mathbf{y}-\mathbf{x}_j| - \left(|\mathbf{y}_0-\mathbf{x}_i| - \gamma_{\boldsymbol{y},\boldsymbol{v},ij}|\mathbf{y}_0-\mathbf{x}_j|\right), \tag{4.27}
$$

$$
\gamma_{\boldsymbol{y},\boldsymbol{v},ij} = \frac{1+\widehat{\mathbf{y}-\mathbf{x}_i}\cdot\mathbf{v}/c_0}{1+\widehat{\mathbf{y}-\mathbf{x}_j}\cdot\mathbf{v}/c_0}. \tag{4.28}
$$

Note that if there is a single transmitter present in the scene, i.e., $M=1$, the second summation in (4.24) vanishes. Thus, similar to the two-receiver case, (4.24) attains its maximum whenever

$$
\frac{\gamma_{\boldsymbol{y},\boldsymbol{v},ij}}{\alpha_{\boldsymbol{y}_0,\boldsymbol{v}_0,\mathbf{x}_j,\mathbf{z}_1}} = \frac{1}{\alpha_{\boldsymbol{y}_0,\boldsymbol{v}_0,\mathbf{x}_i,\mathbf{z}_1}} \tag{4.29}
$$

and $r_{ij} = 0$, i.e.,

$$|\mathbf{y} - \mathbf{x}_i| - \gamma_{\boldsymbol{y},\boldsymbol{v},ij}|\mathbf{y} - \mathbf{x}_j| = |\mathbf{y}_0 - \mathbf{x}_i| - \gamma_{\boldsymbol{y},\boldsymbol{v},ij}|\mathbf{y}_0 - \mathbf{x}_j|, \tag{4.30}$$

where $i = 1, \ldots, N, i \neq j$. Clearly, for $N \geq 3$ and $M = 1$, there are multiple pairs of receivers generating multiple passive-iso-Doppler manifolds, F_{ij}, and passive-iso-range manifolds, R_{ij}, associated with (4.29) and (4.30), respectively. These manifolds intersect at the correct target position and correct target velocity in $(\boldsymbol{y}, \boldsymbol{v})$ space and contribute to the reconstruction of the moving target image. The test-statistic value at the the correct target position and correct target velocity increases by roughly a factor of $N - 1$ as compared to that of the two-receiver case given in (4.4).

If there are multiple transmitters illuminating the scene ($M \geq 2$), under the conditions

$$\frac{\gamma_{\boldsymbol{y},\boldsymbol{v},ij}}{\alpha_{\boldsymbol{y}_0,\boldsymbol{v}_0,\mathbf{x}_j,\mathbf{z}_q}} = \frac{1}{\alpha_{\boldsymbol{y}_0,\boldsymbol{v}_0,\mathbf{x}_i,\mathbf{z}_q}}, \quad q = 1, \ldots, M, \tag{4.31}$$

and

$$\frac{\gamma_{\boldsymbol{y},\boldsymbol{v},ij}}{\alpha_{\boldsymbol{y}_0,\boldsymbol{v}_0,\mathbf{x}_j,\mathbf{z}_q}} = \frac{1}{\alpha_{\boldsymbol{y}_0,\boldsymbol{v}_0,\mathbf{x}_i,\mathbf{z}_{q'}}} \quad q, \quad q' = 1, \ldots, M, \ q \neq q', \tag{4.32}$$

the PSF of the imaging operator in (4.24) can be viewed as the generalized autoambiguity and generalized cross-ambiguity functions of the transmitted waveforms p_q, $q = 1, \ldots, M$, where the generalized auto- and cross-ambiguity functions are interpreted as defined in the previous subsection. The first summation in (4.24) is due to the autoambiguity functions, and the second summation in (4.24) is due to the cross-ambiguity functions of the transmitted waveforms.

Equation (4.31) shows that for M transmitters, there are additional $M - 1$ passive-iso-Doppler manifolds intersecting at the target location and velocity. Therefore, the test-statistic value at the correct target position and correct target velocity increases by roughly a factor of M as compared to that of the single transmitter case.

Note that if (4.32) is satisfied, the terms in the second summation in (4.24) peak at

$$r_{ij} = \frac{\gamma_{\boldsymbol{y},\boldsymbol{v},ij}}{\alpha_{\boldsymbol{y}_0,\boldsymbol{v}_0,\mathbf{x}_j,\mathbf{z}_q}}[c_0(T_{\mathbf{z}_q} - T_{\mathbf{z}_{q'}}) + |\mathbf{y}_0 - \mathbf{z}_{q'}| - |\mathbf{y}_0 - \mathbf{z}_q|]\,. \tag{4.33}$$

Clearly, for $\mathbf{z}_q \neq \mathbf{z}_{q'}$, the passive-iso-Doppler manifolds defined by (4.32) and the passive-iso-range manifolds defined by (4.33) do not intersect at the correct target location and correct target velocity leading to artifacts in the reconstructed image. However, the strength of these artifacts can be weak if the the transmitted waveforms have low correlation. Alternatively, their strength can be suppressed by appropriate design of filters [35].

5. Computational complexity analysis of the moving target imaging algorithm. We use the test-statistic, $\lambda(\boldsymbol{y}, \boldsymbol{v})$, introduced in section 3 to form a four-dimensional image of the scene, which shows the distribution of the targets in the two-dimensional position space as well as their corresponding velocities in the two-dimensional velocity space. To facilitate visualization and performance evaluation, we generate three types of two-dimensional images

from the original four-dimensional image: The fist image, which we refer to as the *peak-value image*, is generated by choosing the maximum value of the four-dimensional image for each velocity (v_1, v_2) to identify the target that has the highest reflectivity. We then choose the maximum value, $\tilde{\boldsymbol{v}}$, of the peak-value image as the estimate of the velocity of this target. The second image, which we refer to as the *position-image*, is the cross-section of the four-dimensional image for $\boldsymbol{v} = \tilde{\boldsymbol{v}}$. We take the maximum value, $\tilde{\boldsymbol{y}}$, of the position-image as the estimate of the target's position. The third image, which we refer to as the *velocity-image*, is the cross-section of the four-dimensional image for $\boldsymbol{y} = \tilde{\boldsymbol{y}}$. Once the target with the largest reflectivity and its corresponding velocity are identified, we can identify the target that has the second largest reflectivity by iteratively forming the peak-value image corresponding to second largest value of the four-dimensional image for each velocity and the corresponding position- and velocity-images. Below we describe the computational complexity of forming the three types of images.

We assume that each measurement has $\mathcal{O}(N)$ samples in time (or frequency) variable and that the range of the position, (y_1, y_2), and velocity, (v_1, v_2), vectors are both discretized into $\mathcal{O}(N \times N)$ samples. For each pair of receivers, the computational complexity of each step of the moving target image formation algorithm is as follows.

(1) *Peak-value image formation.* For each (v_1, v_2) sample, we form the image at (y_1, y_2). The computation of the optimal template and the test-statistic using (3.23) and (3.24), respectively, for each (y_1, y_2) requires $\mathcal{O}(N)$ number of computations. The computational complexity of reconstructing an image for a fix (v_1, v_2) and all (y_1, y_2) is $\mathcal{O}(N^3)$. Thus, for all (v_1, v_2) samples, the computational complexity of forming a four-dimensional image is $\mathcal{O}(N^5)$. Since the computational complexity of calculating the maxima of the four-dimensional image is negligible, the computational complexity of forming the peak-value image is $\mathcal{O}(N^5)$.

(2) *Position-image formation.* Since the position images for each velocity sample are formed in step (1), the position-image for the estimated target velocity is readily available, and, therefore, no computation is needed in this step.

(3) *Velocity-image formation.* For each (v_1, v_2) sample, the optimal template and test-statistic are computed for the estimated target position in $\mathcal{O}(N)$ number of computations. Thus, for all (v_1, v_2), the computational complexity of this step is $\mathcal{O}(N^3)$.

From the analysis above, we conclude that for each pair of receivers, the computational complexity of our imaging method is determined by the four-dimensional and peak-value image formation, $\mathcal{O}(N^5)$, which is proportional to the range and sampling of the velocity and position vectors, and the number of the time (or frequency) samples available in measurements. As the range of the velocity or position vectors increases, or the sampling period of these quantities decreases, the computational complexity of the image formation increases.

Note that our image formation algorithm can be implemented with high efficiency by parallel processing. More specifically, the position images for $N \times N$ velocity samples in (1) can be computed simultaneously resulting in $\mathcal{O}(N^3)$ computations on a single processor. Further reduction in computational complexity at each processor can be attained by exploiting

Fourier domain implementation of the correlation via fast Fourier transform based algorithms.

6. Numerical simulations.

6.1. Simulation parameters and performance evaluation. We conducted numerical simulations to demonstrate the performance of our passive imaging method using a moving point target model. We assumed that there is a single transmitter present in the scene and conducted the simulations with different numbers of receivers and different types of waveforms. In all the experiments, we simulated the thermal noise as an additive white Gaussian process.

We formed the four-dimensional test-statistic image in $((y_1, y_2)\times(v_1, v_2))$ coordinates using the peak-value image and the position- and velocity-images. We performed the performance evaluation using the position- and velocity-images.

6.1.1. Waveforms of opportunity. Taking into account the types of waveforms available in practice as illuminators of opportunity, we used two types of transmitted waveforms in our simulations: The first type of waveforms has high Doppler resolution and relatively poor range resolution, such as frequency modulated (FM) radio and television signals and waveforms used by global system for mobile communication (GSM). We refer to such waveforms as the high-Doppler resolution waveforms. We simulated a high-Doppler resolution waveform as a single-frequency continuous wave (CW) with 4GHz carrier frequency and 0.1s duration in our experiments. Such a waveform provides a radial velocity resolution of about 0.375 m/s in monostatic operations. The second type of waveforms we considered has not only good Doppler resolution but also acceptable range resolution. Examples of such waveforms include wireless network (or WiFi) signals, digital video broadcasting terrestrial (DVB-T) signals, and WiMAX [30] waveforms, which have relatively large bandwidth that can offer reasonable range resolution. We refer to such waveforms as the high-Doppler and good-range resolution waveforms. We simulated a high-Doppler and good-range resolution waveform with the same carrier frequency and duration as the high-Doppler resolution waveform, but with an additional frequency modulation, which results in a bandwidth of 7.5MHz. Such a waveform provides about 19.5 m range resolution and 0.375 m/s radial velocity resolution in monostatic operations.

6.1.2. Position and velocity parameters, and the number and location of receivers. We considered a scene of size $[0, 3e3] \times [0, 3e3]\,\mathrm{m}^2$ with flat topography. We discretized the scene into 201×201 pixels where $[0, 0, 0]$ m and $[3e3, 3e3, 0]$ m correspond to the pixels $(1, 1)$ and $(201, 201)$, respectively. We assumed that the target velocity is in the range of $[-20, 20] \times [-20, 20]$ m/s. We discretized the velocity plane into 401×401 pixels where $[-20, -20, 0]$ m and $[20, 20, 0]$ m correspond to the pixels $(1, 1)$ and $(401, 401)$, respectively.

The point target with unit reflectivity was assumed to be located at $[2.5e3 \quad 2e3 \quad 0]^T$ m moving with velocity $[-10, 15]$ m/s.

For each waveform, we performed the image reconstruction with three, five, and ten receivers present around the scene. The single transmitter was assumed to be located at $[1.5e3, 0, 6]^T$ m. Both the transmitter and receivers were assumed to be on the same z-plane, $z = 6$. The receivers were assumed to lie on the x-axis, equidistant from each other in the range of $[0, 3e3]^T$ m for the three-receiver and the five-receiver cases. For the ten-receiver case, the receivers were distributed around the scene. Figure 6(a) shows the scene with the

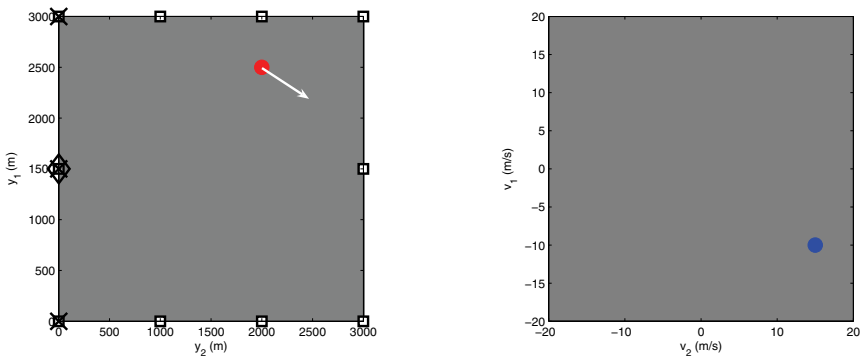

(a) (b)

Figure 6. *The two-dimensional view of the simulation set-up.* (a) *Scene settings for three and ten receivers and a single transmitter. The gray region denotes the scene considered in all the numerical simulations. The red dot indicates the location of the point target with the arrow denoting the direction of the target velocity. The cross signs along the x-axis show the location of the receivers for the three-receiver case, while the blank squares show the location of the receivers for the ten-receiver case. The diamond indicates the location of the transmitter.* (b) *Velocity setting of the moving point target where the target velocity is indicated by a blue dot.*

moving point target, the transmitter, and the receivers for the three- and ten-receiver cases. Figure 6(b) shows the moving target on the velocity plane.

6.1.3. Performance evaluation. We investigated the performance of our imaging method at different levels of SNR of the received signal and with different numbers of receivers using the high-Doppler resolution waveform and the high-Doppler and good-range resolution waveform described above.

We define the SNR of the received signal, SNR_m, as follows:

$$\mathrm{SNR}_m = 20\log_{10}\frac{|\mathrm{E}\,[m]\,|}{\sigma_n}, \tag{6.1}$$

where σ_n denotes the standard deviation of the additive thermal noise.

We use the target-to-background ratio (TBR) as a figure of merit to evaluate the quality of the reconstructed position- and velocity-images. We define the TBR of the position-image and velocity-image, TBR_p and TBR_v, as follows:

$$\mathrm{TBR}_{p(v)} = 20\log_{10}\frac{|\mathrm{E}\left[I_{p(v)}|\mathcal{H}_1\right] - \mathrm{E}\left[I_{p(v)}|\mathcal{H}_0\right]\,|}{\sqrt{\mathrm{Var}[I_{p(v)}|\mathcal{H}_1] + \mathrm{Var}[I_{p(v)}|\mathcal{H}_0]}}, \tag{6.2}$$

where $I_{p(v)}$ denotes the reconstructed position-image or velocity-image. Note that TBR represents the contrast-to-noise ratio of reconstructed images and is consistent with the figure of merit we use in designing the optimal template for the image formation.

We estimated the $\mathrm{TBR}_{p(v)}$ using 20 images, each reconstructed using a different realization of the received signal at a fixed SNR_m. We estimated the $\mathrm{E}\left[I_{p(v)}|\mathcal{H}_1\right]$ by taking a small square area around the target location or target velocity and averaging the values over all the pixels in

the square and over 20 different reconstructions. Similarly, we estimated $\mathrm{E}\left[I_{p(v)}|\mathcal{H}_0\right]$ by taking a small square area of the background where no target was present. The same method was used to estimate the variances. We computed the TBR for different noise levels corresponding to the SNR_m value ranging from -5dB to 12dB.

6.2. Results using the high-Doppler resolution waveform. We used the high-Doppler resolution waveform described in section 6.1.1 in the simulation experiment. The reconstructed images of the moving point target using a single transmitter and three, five, and ten receivers are shown in Figures 7, 8, and 9, respectively.

Figures 7(a), 8(a), and 9(a) show the peak-value images formed using three, five, and ten receivers, respectively. The maximum value of the peak-value image, which corresponds to the estimated velocity, $\tilde{\boldsymbol{v}}$, is indicated by a circle. Figures 7(b), 8(b), and 9(b) show the corresponding position-images (cross-section of the four-dimensional image) when $\boldsymbol{v} = \tilde{\boldsymbol{v}}$. The maximum value of the position-image, which corresponds to the estimated position, $\tilde{\boldsymbol{y}}$, is indicated by a red circle. For ease of comparison, the true position of the target is indicated by a solid red dot. Figures 7(c), 8(c), and 9(c) show the corresponding velocity-images (cross-section of the four-dimensional image) when $\boldsymbol{y} = \tilde{\boldsymbol{y}}$. The maximum value of the velocity-image, i.e., the estimated velocity, is indicated by a blue circle. The true velocity is indicated by a solid blue dot. Note that if the estimated value is almost equal to the true value, only the marker for true value is shown.

Figure 7(a) shows that, with three receivers, ambiguities are present in the peak-value image, indicated by the brightest (dark red) region in the image that spreads in the range of $[-16, -12]$m/s in $\boldsymbol{v}_1$ and the entire range of v_2. Due to the strong ambiguities, the estimated velocity $\tilde{\boldsymbol{v}} = (-13, 15)$m/s deviates from the correct value as expected. The estimated position of the target, $(2580, 2595)$m, has an error as well, as shown by the bright spot in Figure 7(b).

The existence of the ambiguities is related to the velocity resolution of the imaging operator. As can be seen from Figure 7(c), the velocity-image, which is the sum of the two velocity-related passive-iso-Doppler contours formed by each pair of receivers, is ridge-like. Note that the velocity-related passive-iso-Doppler contours are straight lines as described in section 4. The intersection of the two lines contributes to the reconstruction of the target velocity. However, relatively strong ambiguities are present along the ridges. Comparing Figure 7(c) with Figure 7(a), we see that the ambiguities in the peak-value image are related to the ambiguities embedded in the velocity-image.

When the number of receivers increases, additional velocity-related passive-iso-Doppler contours intersect at the correct target velocity, resulting in increased test-statistic value and, thus, improved velocity resolution as shown in Figures 8(c) and 9(c). Although the velocity-images are still ridge-like, the ambiguities along the ridges are much weaker as compared to those of the three-receiver case. This, in return, weakens the ambiguities in the peak-value image, as shown in Figures 8(a) and 9(a).

Note that, in addition to the number of the receivers, the location of the receivers (and the transmitter) also plays a role in the reconstruction performance. For the ten-receiver case, where the receivers were surrounding the scene, the resolution is significantly improved as shown in Figure 9 compared to the five- and three-receiver cases. The velocity-image and the peak-value image are both delta-like, indicating good resolution in both velocity and position.

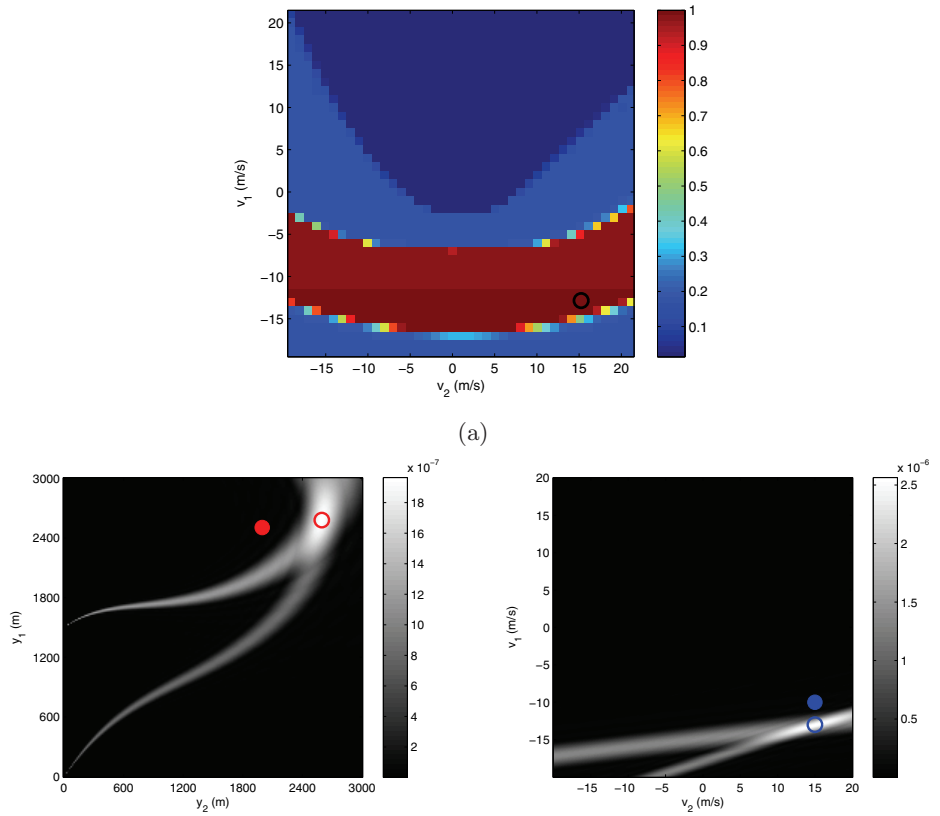

Figure 7. *The reconstructed images for a moving point target with three receivers and a single transmitter transmitting a high-Doppler resolution waveform:* (a) *The peak-value image with the maximum value indicated by the circle. The estimated velocity* $\tilde{\boldsymbol{v}} = (-13, 15)$m/s. (b) *The position-image when* $\boldsymbol{v} = \tilde{\boldsymbol{v}}$. *The estimated position* $\tilde{\boldsymbol{y}} = (2580, 2595)$m. (c) *The velocity-image when* $\boldsymbol{y} = \tilde{\boldsymbol{y}}$. *Solid dots indicate the true position (or velocity), and circles indicate the estimated position (or velocity).*

Since a high-Doppler resolution waveform was used in this set of simulations, the performance of the position-image is mainly determined by the spread of the position-related passive-iso-Doppler curves as expected. As can be seen from the reconstructed position-images in Figures 7(b), 8(b), and 9(b), the position-images are the superposition of the position-related passive-iso-Doppler curves, which intersect at the correct target location. This is consistent with our analysis in section 4. Similar to the reconstructed velocity-images, the strength of the position-image at the correct target location increases with the increasing number of receivers, which results in improved position resolution.

Figures 10(a) and 10(b) show the TBR of the reconstructed position- and velocity-images versus the SNR_m for different numbers of receivers, respectively. We see that both TBR_p and TBR_v increase with the increasing number of receivers. This is consistent with the improvement observed in the reconstructed images as shown in Figures 7–9.

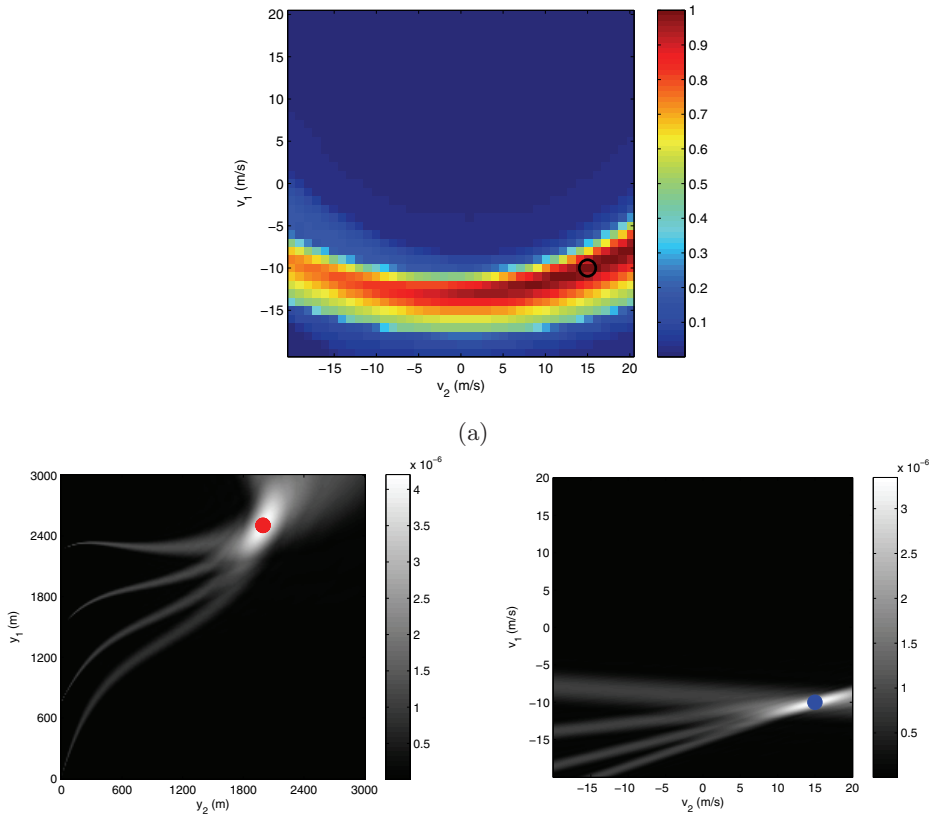

Figure 8. *The reconstructed images for a moving point target with five receivers and a single transmitter transmitting a high-Doppler resolution waveform:* (a) *The peak-value image with the maximum value indicated by a circle. The estimated velocity* $\tilde{\boldsymbol{v}} = (-10, 15)$m/s. (b) *The position-image when* $\boldsymbol{v} = \tilde{\boldsymbol{v}}$. *The estimated position* $\tilde{\boldsymbol{y}} = (2500, 2000)$m. (c) *The velocity-image when* $\boldsymbol{y} = \tilde{\boldsymbol{y}}$. *Solid dots indicate the true position (or velocity), and circles indicate the estimated position (or velocity).*

6.3. Results using the high-Doppler and good-range resolution waveform. We conducted numerical simulations using the high-Doppler and good-range resolution waveform described above and three, five, and ten receivers. The corresponding reconstructed images are shown in Figures 11, 12, and 13. As before, we use circles to indicate the estimated positions (or velocities) and solid dots to indicate the true positions (or velocities).

The peak-value images are shown in Figures 11(a), 12(a), and 13(a) with circles indicating the estimated velocity $\tilde{\boldsymbol{v}}$. The position-images, as shown in Figures 11(b), 12(b), and 13(b), are the cross-sections of the four-dimensional images for $\boldsymbol{v} = \tilde{\boldsymbol{v}}$, while the velocity-images, as shown in Figures 11(c), 12(c), and 13(c), are the cross-sections of the four-dimensional images for $\boldsymbol{y} = \tilde{\boldsymbol{y}}$.

Figures 11(b)(c), 12(b)(c), and 13(b)(c) show that, similar to the results obtained using a high-Doppler resolution waveform, both the position and velocity resolutions improve as the

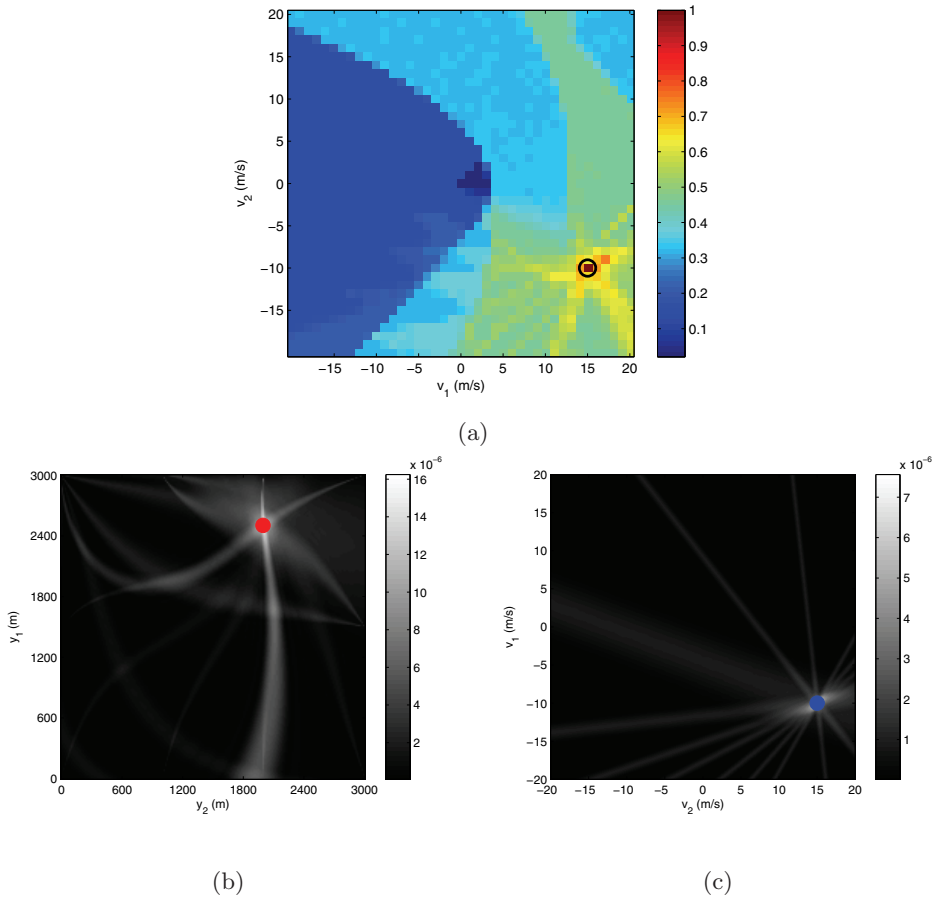

Figure 9. *The reconstructed images for a moving point target with ten receivers and a single transmitter transmitting a high-Doppler resolution waveform:* (a) *The peak-value image with the maximum value indicated by a circle. The estimated velocity* $\tilde{\boldsymbol{v}} = (-10, 15)$m/s. (b) *The position-image when* $\boldsymbol{v} = \tilde{\boldsymbol{v}}$. *The estimated position* $\tilde{\boldsymbol{y}} = (2500, 2000)$m. (c) *The velocity-image when* $\boldsymbol{y} = \tilde{\boldsymbol{y}}$. *Solid dots indicate the true position (or velocity), and circles indicate the estimated position (or velocity).*

number of receivers increases. Also, the improvement in the velocity resolution weakens the ambiguities in the peak-value images, as can be seen in Figures 11(a), 12(a), and 13(a).

Additionally, we observe that the velocity estimates obtained using the two different waveforms are almost the same when the images in Figures 11(c), 12(c), and 13(c) are compared with the images in Figures 7(c), 8(c), and 9(c). This is consistent with our analysis in section 4, which states that the velocity resolution depends only on the Doppler ambiguity of the transmitted waveform.

Furthermore, comparing the images in Figures 11(b), 12(b), and 13(b) with those in Figures 7(b), 8(b), and 9(b), we observe that the position-images obtained using the high-Doppler and good-range resolution waveform are not simply the sum of the position-related passive-iso-Doppler curves due to the good-range ambiguity provided by the waveform. For this type of waveform, multiple passive-iso-range manifolds along with multiple passive-iso-

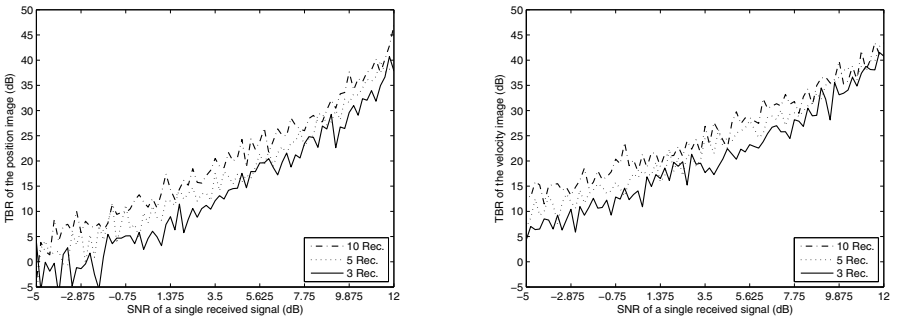

(a) (b)

Figure 10. *TBR versus* SNR_m *for* (a) *position-images and* (b) *velocity-images obtained with different numbers of receivers and a single transmitter transmitting a high-Doppler resolution waveform.*

Doppler manifolds contribute to the intersection at the correct target position. As a result, the projection of the intersection onto the position plane is no longer simply the position-related passive-iso-Doppler or the position-related passive-iso-range curves, as can be observed in Figures 11(b), 12(b), and 13(b). This result is consistent with our analysis in section 4.1.3.

The TBR of the position- and velocity-images versus the SNR_m for different numbers of receivers is shown in Figures 14(a) and 14(b), respectively. We see that both TBR_p and TBR_v increase with the increasing number of receivers, as expected.

7. Conclusion. In this work, we presented a new passive imaging method for moving targets in position and velocity spaces using sparsely distributed receivers and noncooperative transmitters of opportunity. Our imaging method is comprised of a novel passive measurement model for moving targets and an associated image formation method. We defined the concept of passive-Doppler-scale-factor and developed a passive measurement model to relate the Doppler and delay information measured at different receiver locations. We next formulated the passive image formation problem within a GLRT framework where we set up a test of binary hypotheses using the passive measurement model for a hypothetical target located at an unknown position, moving with an unknown velocity. We designed a linear discriminant functional by maximizing the SNR of the test-statistic. The resulting discriminant functional correlates the filtered, delayed, and scaled (or dilated) averaged measurements from one receiver location with the measurements at another receiver location where the filtering is determined by the additive noise statistics, the delay is determined by the hypothetical target position, and the dilation is determined by the hypothetical passive-Doppler-scale-factor.

We presented the resolution analysis of our passive imaging algorithm in position and velocity spaces. Our analysis shows that the resolution in position and velocity spaces is determined by the intersection of the passive-iso-Doppler and passive-iso-range manifolds whose spread is associated with the underlying Doppler and range ambiguity functions of the waveforms of opportunity.

We presented computational complexity of our imaging algorithm and extensive simulation results to verify our analysis and to demonstrate the performance of our passive imaging method using different waveforms of opportunity available in the real world.

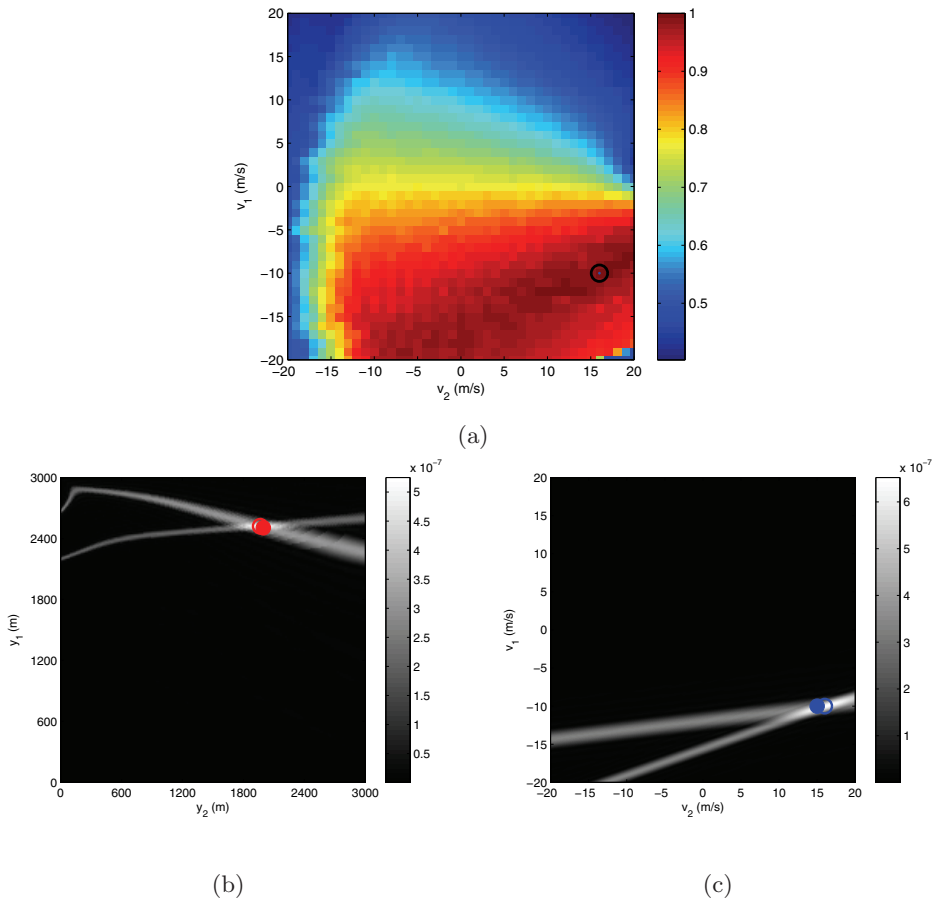

Figure 11. *The reconstructed images for a moving point target with three receivers and a single transmitter transmitting a high-Doppler and good-range resolution waveform.* (a) *The peak-value image with the maximum value indicated by a circle. The estimated velocity* $\tilde{\boldsymbol{v}} = (-10, 16)$m/s. (b) *The position-image with* $\boldsymbol{v} = \tilde{\boldsymbol{v}}$. *The estimated position* $\tilde{\boldsymbol{y}} = (2520, 1965)$m. (c) *The velocity-image with* $\boldsymbol{y} = \tilde{\boldsymbol{y}}$. *Solid dots indicate the true position (or velocity), and circles indicate the estimated position (or velocity).*

Unlike the existing passive moving target detection methods, our imaging method can determine the two- or three-dimensional velocity vector as well as the two- or three-dimensional position vector of a moving target, as opposed to only the radial position and velocity estimates. Our passive moving target imaging model can be utilized for target tracking when combined with a dynamic a priori model. Additionally, our passive measurement model can be extended to sparse apertures operating in multiple-scattering environments.

Our method assumes that the receivers are synchronized with respect to a common reference clock and that the locations of the receivers are known. Any error in the synchronization of receivers or lack of full knowledge of their location will result in a lack of focus in the reconstructed position and velocity space images, similar to the type that arises in the well-known autofocus problem [5, 21]. This problem may be addressed by adapting the autofocus techniques to the passive imaging problems.

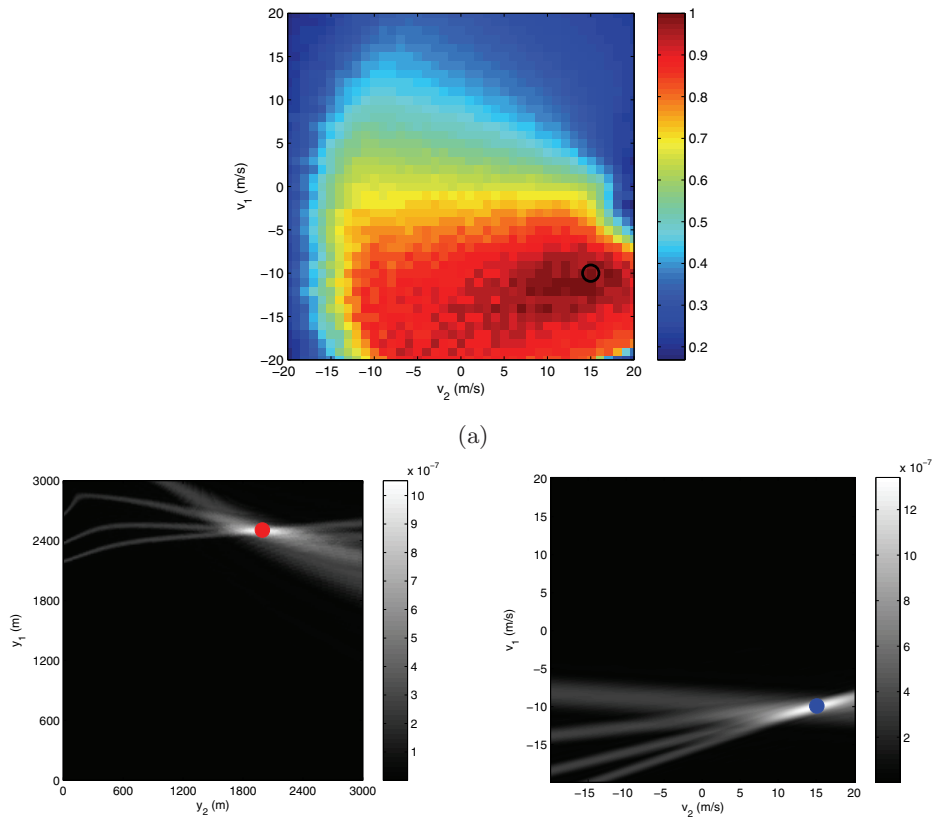

(a)

(b) (c)

Figure 12. *The reconstructed images for a moving point target with five receivers and a single transmitter transmitting a high-Doppler and good-range resolution waveform.* (a) *The peak-value image with the maximum value indicated by a circle. The estimated velocity* $\tilde{\boldsymbol{v}} = (-10, 15)$m/s. (b) *The position-image with* $\boldsymbol{v} = \tilde{\boldsymbol{v}}$. *The estimated position* $\tilde{\boldsymbol{y}} = (2500, 2000)$m. (c) *The velocity-image with* $\boldsymbol{y} = \tilde{\boldsymbol{y}}$. *Solid dots indicate the true position (or velocity), and circles indicate the estimated position (or velocity).*

Finally, we note that the passive moving target imaging method introduced in this paper is not limited to radar and can be easily adapted to similar passive moving object imaging problems in acoustics, geophysics, or microwave imaging.

Appendix A. Derivation of the optimal linear template. We begin with the objective functional in (3.18). The numerator of (3.18) can be expressed as

$$|\langle \mathbf{P}_{\boldsymbol{y},\boldsymbol{v}} \overline{\mathbf{m}}_{\mathbf{r}}, \mathbf{w} \rangle|^2 = \langle \mathbf{P}_{\boldsymbol{y},\boldsymbol{v}} \overline{\mathbf{m}}_{\mathbf{r}}, \mathbf{w} \rangle \langle \mathbf{w}, \mathbf{P}_{\boldsymbol{y},\boldsymbol{v}} \overline{\mathbf{m}}_{\mathbf{r}} \rangle \tag{A.1}$$

$$= \int \mathbf{w}^H \underbrace{\mathbf{P}_{\boldsymbol{y},\boldsymbol{v}} \overline{\mathbf{m}}_{\mathbf{r}} \overline{\mathbf{m}}_{\mathbf{r}}^H \mathbf{P}_{\boldsymbol{y},\boldsymbol{v}}^H}_{\mathbf{R}_G} \mathbf{w} d\omega d\omega' \tag{A.2}$$

$$=: \langle \mathcal{R}_G \mathbf{w}, \mathbf{w} \rangle , \tag{A.3}$$

where $\mathcal{R}_G$ is a nonnegative definite symmetric operator with kernel $\mathbf{R}_G$. $J(\mathbf{w})$ is maximized

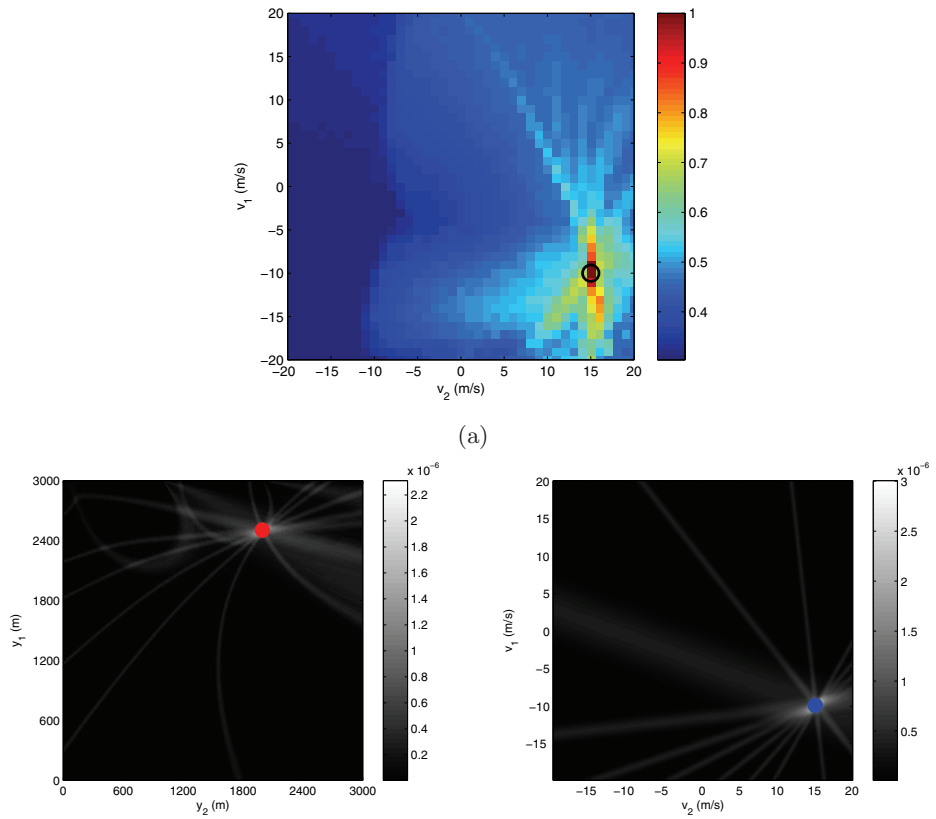

Figure 13. *The reconstructed images for a moving point target with ten receivers and a single transmitter transmitting a high-Doppler and good-range resolution waveform.* (a) *The peak-value image with the maximum value indicated by a circle. The estimated velocity* $\tilde{\boldsymbol{v}} = (-10, 15)$m/s. (b) *The position-image with* $\boldsymbol{v} = \tilde{\boldsymbol{v}}$. *The estimated position* $\tilde{\boldsymbol{y}} = (2500, 2000)$m. (c) *The velocity-image with* $\boldsymbol{y} = \tilde{\boldsymbol{y}}$. *Solid dots indicate the true position (or velocity), and circles indicate the estimated position (or velocity).*

by taking the Fréchet derivative of (3.18) with respect to $\mathbf{w}$. To do so we apply the chain rule. The Fréchet derivative of $\langle \mathcal{R}\mathbf{w}, \mathbf{w}\rangle$, where $\mathcal{R}$ is some symmetric nonnegative definite bounded linear operator, can be obtained by straightforward application of the Gâteaux derivative:

$$Df(\mathbf{w}) = \lim_{t\to 0} \frac{\langle \mathcal{R}(\mathbf{w}+t\mathbf{h}), \mathbf{w}+t\mathbf{h}\rangle - \langle \mathcal{R}\mathbf{w}, \mathbf{w}\rangle}{t} \tag{A.4}$$

$$= \langle \mathcal{R}\mathbf{w}, \mathbf{h}\rangle + \langle \mathcal{R}\mathbf{h}, \mathbf{w}\rangle = \langle \mathcal{R}\mathbf{w}, \mathbf{h}\rangle + \overline{\langle \mathcal{R}\mathbf{w}, \mathbf{h}\rangle} \tag{A.5}$$

$$= 2\mathtt{Re}\{\langle \mathcal{R}\mathbf{w}, \mathbf{h}\rangle\}. \tag{A.6}$$

The above holds for all $\mathbf{h} \in L^2 \times \mathbb{R}^M$, and thus by the Riesz–Fréchet theorem, $Df(\mathbf{w}) = 2\Re\{\langle \mathcal{R}\mathbf{w}, \cdot\rangle\}$ is a linear functional on the function space $L^2 \times \mathbb{R}^M$. For notational simplicity, we denote $\langle \mathcal{R}\mathbf{w}, \cdot\rangle$ with $\mathcal{R}\mathbf{w}$.

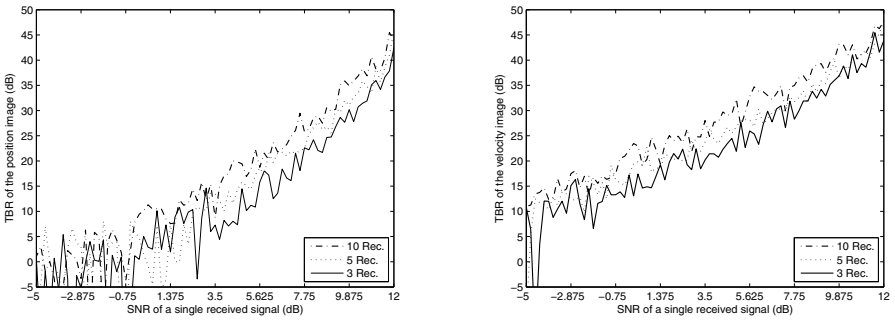

(a) (b)

Figure 14. *TBR versus* SNR_m *for* (a) *position-images and* (b) *velocity-images obtained with different numbers of receivers and a single transmitter transmitting a high-Doppler and good-range resolution waveform.*

Using (A.4), the Fréchet derivative of (3.18) is given by

$$DJ(\mathbf{w}) = \frac{2\mathtt{Re}\{\mathcal{R}_{\mathtt{G}}\mathbf{w}\}}{\langle\overline{\mathcal{R}}\mathbf{w},\mathbf{w}\rangle} - \frac{2\mathtt{Re}\{\overline{\mathcal{R}}\mathbf{w}\}\,\langle\mathcal{R}_{\mathtt{G}}\mathbf{w},\mathbf{w}\rangle}{\left(\langle\overline{\mathcal{R}}\mathbf{w},\mathbf{w}\rangle\right)^2} \tag{A.7}$$

$$= \frac{2\mathtt{Re}\{\mathcal{R}_{\mathtt{G}}\mathbf{w}\} - 2\mathtt{Re}\{\overline{\mathcal{R}}\mathbf{w}\}\mathtt{J}(\mathbf{w})}{\langle\overline{\mathcal{R}}\mathbf{w},\mathbf{w}\rangle}. \tag{A.8}$$

By setting $DJ(w) = 0$ and rearranging the terms, we get the following generalized eigenvalue problem:

$$\mathcal{R}_G\mathbf{w} = J(\mathbf{w})\overline{\mathcal{R}}\mathbf{w}. \tag{A.9}$$

By the form of $\mathbf{R}_G$, defined in (A.2), the eigenfunction of $\mathcal{R}_G$ is proportional to $\mathbf{P}_{\boldsymbol{y},\boldsymbol{v}}\overline{\mathbf{m}}_{\mathbf{r}}$, and so, assuming $\overline{\mathcal{R}}$ is invertible, the optimal linear detector is proportional to

$$\mathbf{w}_{\mathrm{opt}} = \overline{\mathcal{R}}^{-1}\mathbf{P}_{\boldsymbol{y},\boldsymbol{v}}\overline{\mathbf{m}}_{\mathbf{r}}. \tag{A.10}$$

Appendix B. Proof of the diagonal approximation of $\overline{\mathbf{S}}^{-1}$. Using (3.21) and (3.16), under the wide-sense stationary assumption of the noise at each receiver, we obtain

$$\overline{\mathbf{S}}(\omega) = \frac{1}{2}\mathbf{P}_{\boldsymbol{y},\boldsymbol{v}}(\omega)\mathbf{R}_{\mathbf{n_r}}(\omega)\mathbf{P}^H_{\boldsymbol{y},\boldsymbol{v}}(\omega) + \mathbf{R}_{\mathbf{n}}(\omega). \tag{B.1}$$

For notational simplicity, we drop the ω dependence and the subscripts $\boldsymbol{y}$ and $\boldsymbol{v}$ of $\mathcal{P}$ for the rest of our treatment.

For clarity of exposition, we assume that there are three receivers present in the scene and take the first as the reference. Then, using (2.43), (3.2), and (3.3), under the assumption that the noise at different receivers is uncorrelated, we have

$$\overline{\mathbf{S}} = \begin{bmatrix} \frac{1}{2}|\mathcal{P}_2\mathcal{P}_1^{-1}|^2 S_n^1 + S_n^2 & \frac{1}{2}\mathcal{P}_2\mathcal{P}_1^{-1}(\mathcal{P}_3\mathcal{P}_1^{-1})^* S_n^1 \\ \frac{1}{2}\mathcal{P}_3\mathcal{P}_1^{-1}(\mathcal{P}_2\mathcal{P}_1^{-1})^* S_n^1 & \frac{1}{2}|\mathcal{P}_3\mathcal{P}_1^{-1}|^2 S_n^1 + S_n^3 \end{bmatrix}, \tag{B.2}$$

where S_n^i denotes the power spectral density function of the noise at the ith receiver, $i = 1, 2, 3$, and $|\mathcal{P}_i\mathcal{P}_j^{-1}|^2 = \mathcal{P}_i\mathcal{P}_j^{-1}(\mathcal{P}_i\mathcal{P}_j^{-1})^*$ for $i = 2, 3$ and $j = 1$.

The inverse of $\overline{\mathbf{S}}$ has the form

$$\overline{\mathbf{S}}^{-1} = \frac{1}{|\overline{\mathbf{S}}|}\begin{bmatrix} \frac{1}{2}|\mathcal{P}_3\mathcal{P}_1^{-1}|^2 S_n^1 + S_n^3 & -\frac{1}{2}\mathcal{P}_2\mathcal{P}_1^{-1}(\mathcal{P}_3\mathcal{P}_1^{-1})^* S_n^1 \\ \frac{1}{2}\mathcal{P}_3\mathcal{P}_1^{-1}(\mathcal{P}_2\mathcal{P}_1^{-1})^* S_n^1 & \frac{1}{2}|\mathcal{P}_2\mathcal{P}_1^{-1}|^2 S_n^1 + S_n^2 \end{bmatrix}, \tag{B.3}$$

where $|\overline{\mathbf{S}}|$ denotes the determinant of $\overline{\mathbf{S}}$.

Substituting (B.3) into (3.22), we obtain

$$\begin{aligned} \mathbf{w}_{\text{opt}} &= \frac{1}{|\overline{\mathbf{S}}|}\begin{bmatrix} \frac{1}{2}S_n^1|\mathcal{P}_3\mathcal{P}_1^{-1}|^2 + S_n^3 & -\frac{1}{2}S_n^1\mathcal{P}_2\mathcal{P}_1^{-1}(\mathcal{P}_3\mathcal{P}_1^{-1})^* \\ \frac{1}{2}S_n^1\mathcal{P}_3\mathcal{P}_1^{-1}(\mathcal{P}_2\mathcal{P}_1^{-1})^* & \frac{1}{2}S_n^1|\mathcal{P}_2\mathcal{P}_1^{-1}|^2 + S_n^2 \end{bmatrix} \\ &\qquad \times \begin{bmatrix} \mathcal{P}_2\mathcal{P}_1^{-1} & 0 \\ 0 & \mathcal{P}_3\mathcal{P}_1^{-1} \end{bmatrix}\begin{bmatrix} \bar{\hat{m}}_1 \\ \bar{\hat{m}}_1 \end{bmatrix} \\ &= \frac{1}{|\overline{\mathbf{S}}|}\begin{bmatrix} \left(\frac{1}{2}S_n^1|\mathcal{P}_3\mathcal{P}_1^{-1}|^2\mathcal{P}_2\mathcal{P}_1^{-1} + S_n^3\mathcal{P}_2\mathcal{P}_1^{-1} - \frac{1}{2}S_n^1\mathcal{P}_2\mathcal{P}_1^{-1}|\mathcal{P}_3\mathcal{P}_1^{-1}|^2\right)\bar{\hat{m}}_1 \\ \left(-\frac{1}{2}S_n^1\mathcal{P}_3\mathcal{P}_1^{-1}|\mathcal{P}_2\mathcal{P}_1^{-1}|^2 + \frac{1}{2}S_n^1|\mathcal{P}_2\mathcal{P}_1^{-1}|^2\mathcal{P}_3\mathcal{P}_1^{-1} + S_n^2\mathcal{P}_3\mathcal{P}_1^{-1}\right)\bar{\hat{m}}_1 \end{bmatrix}. \end{aligned} \tag{B.4}$$

Note that if

$$|\mathcal{P}_i\mathcal{P}_j^{-1}|^2\mathcal{P}_m\mathcal{P}_j^{-1} = \mathcal{P}_m\mathcal{P}_j^{-1}|\mathcal{P}_i\mathcal{P}_j^{-1}|^2, \tag{B.5}$$

where $j = 1$, $i, m = 2, 3$, and $m \neq i$, (B.4) becomes

$$\mathbf{w}_{\text{opt}} = \frac{1}{|\overline{\mathbf{S}}|}\begin{bmatrix} S_n^3\mathcal{P}_2\mathcal{P}_1^{-1}\bar{\hat{m}}_1 \\ S_n^2\mathcal{P}_3\mathcal{P}_1^{-1}\bar{\hat{m}}_1 \end{bmatrix}, \tag{B.6}$$

which shows that $\overline{\mathbf{S}}^{-1}$ is a diagonal matrix given by

$$\overline{\mathbf{S}}^{-1} = \frac{1}{|\overline{\mathbf{S}}|}\begin{bmatrix} S_n^3 & 0 \\ 0 & S_n^2 \end{bmatrix}. \tag{B.7}$$

Similar to the derivation above, it can be shown that $\overline{\mathbf{S}}^{-1}$ can be reduced to a diagonal matrix for the case of $N > 3$ receivers as long as (B.5) holds for $i, m = 1, \ldots, N$, and $i, m \neq j$, $i \neq m$, where the jth receiver is used as the reference.

Let

$$\mathcal{Q}_{n,i,m} = (\mathcal{P}_n\mathcal{P}_j^{-1})(\mathcal{P}_i\mathcal{P}_j^{-1})^*(\mathcal{P}_m\mathcal{P}_j^{-1}). \tag{B.8}$$

Thus, (B.5) can be written as

$$\mathcal{Q}_{i,i,m} = \mathcal{Q}_{m,i,i}. \tag{B.9}$$

Using (2.35), (2.36), and (2.21), we obtain

$$\mathcal{P}_n\mathcal{P}_j^{-1}[\hat{f}](\omega) = \frac{|\mathbf{y} - \mathbf{x}_j|}{|\mathbf{y} - \mathbf{x}_i|}\frac{\mu_i}{\mu_j}\hat{f}\left(\frac{\mu_i}{\mu_j}\omega\right)\mathrm{e}^{\mathrm{i}\frac{\mu_i}{\mu_j}k|\mathbf{y}-\mathbf{x}_j|}\mathrm{e}^{-\mathrm{i}k|\mathbf{y}-\mathbf{x}_i|}. \tag{B.10}$$

Letting $\tilde{f} = \mathcal{P}_n\mathcal{P}_j^{-1}[\hat{f}](\omega)$, we obtain $(\mathcal{P}_n\mathcal{P}_j^{-1})^*[\hat{f}] = \tilde{f}^*$. In (B.10) μ is as defined in (2.17). (We drop the subscripts $\boldsymbol{y}$ and $\boldsymbol{v}$ from μ for notational simplicity.)

Using (B.10), we express (B.8) as

$$\begin{aligned}\mathcal{Q}_{n,i,m}[\hat{f}](\omega) &= (\mathcal{P}_n\mathcal{P}_j^{-1})(\mathcal{P}_i\mathcal{P}_j^{-1})^*(\mathcal{P}_m\mathcal{P}_j^{-1})[\hat{f}](\omega)\\ &= \frac{|\mathbf{y}-\mathbf{x}_j|^3}{|\mathbf{y}-\mathbf{x}_n||\mathbf{y}-\mathbf{x}_i||\mathbf{y}-\mathbf{x}_m|}\frac{\mu_n\mu_i\mu_m}{\mu_j^3}\hat{f}\left(\frac{\mu_n\mu_i\mu_m}{\mu_j^3}\omega\right)\mathrm{e}^{\mathrm{i}\frac{\mu_n\mu_i\mu_m}{\mu_j^3}k|\mathbf{y}-\mathbf{x}_j|}\\ &\quad\times\mathrm{e}^{-\mathrm{i}\frac{\mu_n\mu_i}{\mu_j^2}k|\mathbf{y}-\mathbf{x}_m|}\mathrm{e}^{-\mathrm{i}\frac{\mu_n\mu_i}{\mu_j^2}k|\mathbf{y}-\mathbf{x}_j|}\mathrm{e}^{\mathrm{i}\frac{\mu_n}{\mu_j}k|\mathbf{y}-\mathbf{x}_i|}\mathrm{e}^{\mathrm{i}\frac{\mu_n}{\mu_j}k|\mathbf{y}-\mathbf{x}_j|}\mathrm{e}^{-\mathrm{i}k|\mathbf{y}-\mathbf{x}_n|}.\end{aligned}\tag{B.11}$$

Thus, the left-hand side of (B.9) becomes

$$\begin{aligned}\mathcal{Q}_{i,i,m}[\hat{f}](\omega) &= \frac{|\mathbf{y}-\mathbf{x}_j|^3}{|\mathbf{y}-\mathbf{x}_i|^2|\mathbf{y}-\mathbf{x}_m|}\frac{\mu_i^2\mu_m}{\mu_j^3}\hat{f}\left(\frac{\mu_i^2\mu_m}{\mu_j^3}\omega\right)\mathrm{e}^{\mathrm{i}\frac{\mu_i^2\mu_m}{\mu_j^3}k|\mathbf{y}-\mathbf{x}_j|}\\ &\quad\times\mathrm{e}^{-\mathrm{i}k\left(\frac{\mu_m(\mu_i-\mu_j)}{\mu_j^2}|\mathbf{y}-\mathbf{x}_j|+\frac{\mu_m(\mu_i-\mu_j)}{\mu_j^2}|\mathbf{y}-\mathbf{x}_i|+|\mathbf{y}-\mathbf{x}_m|\right)},\end{aligned}\tag{B.12}$$

and the right-hand side of (B.9) becomes

$$\begin{aligned}\mathcal{Q}_{m,i,i}[\hat{f}](\omega) &= \frac{|\mathbf{y}-\mathbf{x}_j|^3}{|\mathbf{y}-\mathbf{x}_i|^2|\mathbf{y}-\mathbf{x}_m|}\frac{\mu_i^2\mu_m}{\mu_j^3}\hat{f}\left(\frac{\mu_i^2\mu_m}{\mu_j^3}\omega\right)\mathrm{e}^{\mathrm{i}\frac{\mu_i^2\mu_m}{\mu_j^3}k|\mathbf{y}-\mathbf{x}_j|}\\ &\quad\times\mathrm{e}^{-\mathrm{i}k\left(\frac{\mu_i(\mu_i-\mu_j)}{\mu_j^2}|\mathbf{y}-\mathbf{x}_j|+\frac{(\mu_j-\mu_i)}{\mu_j}|\mathbf{y}-\mathbf{x}_i|+\frac{\mu_i^2}{\mu_j^2}|\mathbf{y}-\mathbf{x}_m|\right)}.\end{aligned}\tag{B.13}$$

Recall that in the slow-mover case, where the target speed is much slower than the speed of light, the scaling factor μ is very close to 1. We can then approximate

$$\begin{aligned}&\frac{\mu_i(\mu_i-\mu_j)}{\mu_j^2}|\mathbf{y}-\mathbf{x}_j|+\frac{(\mu_j-\mu_i)}{\mu_j}|\mathbf{y}-\mathbf{x}_i|+\frac{\mu_i^2}{\mu_j^2}|\mathbf{y}-\mathbf{x}_m|\\ &\approx\frac{\mu_m(\mu_i-\mu_j)}{\mu_j^2}|\mathbf{y}-\mathbf{x}_j|+\frac{\mu_m(\mu_i-\mu_j)}{\mu_j^2}|\mathbf{y}-\mathbf{x}_i|+|\mathbf{y}-\mathbf{x}_m|.\end{aligned}\tag{B.14}$$

Thus, (B.13) is approximately equal to (B.12), and therefore (B.5) holds. As a result, $\overline{\mathbf{S}}^{-1}$ can be reduced to a diagonal matrix.

REFERENCES

[1] C. J. Baker, H. D. Griffiths, and I. Papoutsis, *Passive coherent location radar systems. Part 2: Waveform properties*, IEE Proceedings of Radar, Sonar, and Navigation, 152 (2005), pp. 160–168.
[2] H. H. Barrett and K. J. Myers, *Foundations of Image Science*, Wiley-Interscience, New York, 2003.
[3] L. Borcea, G. Papanicolaou, and C. Tsogka, *Interferometric array imaging in clutter*, Inverse Problems, 21 (2005), pp. 1419–1460.

[4] L. Borcea, G. Papanicolaou, and C. Tsogka, *Coherent interferometric imaging in clutter*, Geophysics, 71 (2006), pp. SI165–SI175.
[5] W. D. Brown and D. C. Ghiglia, *Some methods for reducing propagation-induced phase errors in coherent imaging systems. Part* I: *Formalism*, J. Opt. Soc. Amer., 48 (1988), pp. 924–941.
[6] C. C. Chen and H. C. Andrews, *Target motion induced radar imaging*, IEEE Trans. Aerospace Electron. Syst., 16 (1980), pp. 2–14.
[7] M. Cheney, *A mathematical tutorial on synthetic aperture radar*, SIAM Rev., 43 (2001), pp. 301–312.
[8] M. Cheney and B. Borden, *Imaging moving targets from scattered waves*, Inverse Problems, 24 (2008), 035005.
[9] M. Cheney and B. Borden, *Problems in synthetic-aperture radar imaging*, Inverse Problems, 25 (2009), 123005.
[10] M. Cherniakov, K. Kubik, and D. Nezlin, *Bistatic synthetic aperture radar with non-cooperative LEOS based transmitter*, in Proceedings of the IEEE International Geoscience and Remote Sensing Symposium, Honolulu, HI, 2000, pp. 861–862.
[11] M. Cherniakov, R. Saini, R. Zuo, and M. Antoniou, *Space surface bistatic* SAR *with space-borne non-cooperative transmitters*, in Proceedings of the European Radar Conference, Paris, France, 2005, pp. 25–28.
[12] K. Chetty, K. Woodbridge, H. Guo, and G. E. Smith, *Passive bistatic WiMAX radar for marine surveillance*, in Proceedings of the IEEE Radar Conference, Washington, DC, 2010, pp. 188–193.
[13] J. M. Christiansen and K. E. Olsen, *Range and Doppler walk in DVB-T based passive bistatic radar*, in Proceedings of the IEEE Radar Conference, Washington, DC, 2010, pp. 620–626.
[14] C. Coleman and H. Yardley, *Passive bistatic radar based on target illumniations by digital audio broadcasting*, IET Radar Sonar Navig., 2 (2008), pp. 366–375.
[15] D. Colton and R. Kress, *Inverse Acoustic and Electromagnetic Scattering Theory*, 2nd ed., Appl. Math. Sci. 93, Springer, New York, 1998.
[16] G. Derveaux, G. Papanicolaou, and C. Tsogka, *Time reversal imaging for sensor networks with optimal compensation in time*, J. Acoust. Soc. Amer., 121 (2007), pp. 2071–2085.
[17] P. Falcone, F. Colone, C. Bongioanni, and P. Lombardo, *Experimental results for OFDM WiFi-based passive bistatic radar*, in Proceedings of the IEEE Radar Conference, Washington, DC, 2010, pp. 516–521.
[18] J. Garnier, *Imaging in randomly layered media by cross-correlating noisy signals*, Multiscale Model. Simul., 4 (2005), pp. 610–640.
[19] J. Garnier and G. Papanicolaou, *Passive sensor imaging using cross correlations of noisy signals in a scattering medium*, SIAM J. Imaging Sci., 2 (2009), pp. 396–437.
[20] J. Garnier and G. Papanicolaou, *Resolution analysis for imaging with noise*, Inverse Problems, 26 (2010), 074001.
[21] D. C. Ghiglia and W. D. Brown, *Some methods for reducing propagation-induced phase errors in coherent imaging systems. Part* II: *Numerical results*, J. Opt. Soc. Amer., 48 (1988), pp. 942–957.
[22] D. N. Ghosh Roy and L. S. Couchman, *Inverse Problems and Inverse Scattering of Plane Waves*, Academic Press, London, 2002.
[23] H. D. Griffiths and C. J. Baker, *Passive coherent location radar systems. Part* 1: *Performance prediction*, IEE Proceedings of Radar, Sonar and Navigation, 152 (2005), pp. 153–159.
[24] H. D. Griffiths and N. R. W. Long, *Television-based bistatic radar*, IEE Proceedings of Radar, Sonar and Navigation, 133 (1986), pp. 649–657.
[25] H. Guo, K. Woodbridge, and C. J. Baker, *Evaluation of WiFi beacon transmissions for wireless based passive radar*, in Proceedings of the IEEE Radar Conference, Rome, Italy, 2008, pp. 769–774.
[26] H. A. Harms, L. M. Davis, and J. Palmer, *Understanding the signal structure in DVB-T signals for passive radar detection*, in Proceedings of the IEEE Radar Conference, Washington, DC, 2010, pp. 532–537.
[27] X. He, M. Cherniakov, and T. Zeng, *Signal detectability in SS-BSAR with GNSS non-cooperative transmitter*, IEE Proceedings of Radar, Sonar and Navigation, 152 (2005), pp. 124–132.
[28] J. Homer, K. Kubik, B. Mojarrabi, I. Longstaff, E. Donskoi, and M. Cherniakov, *Passive bistatic radar sensing with LEOS based transmitters*, in Proceedings of the IEEE International Geoscience and Remote Sensing Symposium, Toronto, Canada, 2002, pp. 438–440.

[29] P. E. Howland, D. Maksimiuk, and G. Reitsma, *FM radio based bistatic radar*, IEE Proceedings of Radar, Sonar and Navigation, 152 (2005), pp. 107–115.
[30] IEEE, *IEEE Standard* 802.16e-2005 *and IEEE Standard* 802.16-2004/Cor 1-2005, *Part* 16: *Air Interface for Fixed and Mobile Broadband Wireless Access Systems*, IEEE, Washington, DC, 2005.
[31] S. Kay, *Fundamentals of Statistical Signal Processing, Vol.* I: *Estimation Theory*, Prentice–Hall, Englewood Cliffs, NJ, 1993.
[32] S. Kay, *Fundamentals of Statistical Signal Processing, Vol* II: *Detection Theory*, Prentice–Hall, Englewood Cliffs, NJ, 1998.
[33] S. M. Kay, *Fundamentals of Statistical Signal Processing, Vol.* I *and Vol.* II, Prentice–Hall, Englewood Cliffs, NJ, 1998.
[34] V. Koch and R. Westphal, *New approach to a multistatic passive radar sensor for air/space defense*, IEEE Aero. Electron. Syst. Mag., 10 (1995), pp. 24–32.
[35] V. Krishnan, J. Swoboda, C. E. Yarman, and B. Yazici, *Multi-static synthetic aperture radar image formation*, IEEE Trans. Image Process., 19 (2010), pp. 1290–1306.
[36] K. S. Kulpa, *Multi-static entirely passive detection of moving targets and its limitations*, IEE Proceedings of Radar, Sonar, and Navigation, 152 (2005), pp. 169–173.
[37] F. S. M. W. L. Lo Monte and D. Erricolo, *Radio frequency tomography for tunnel detection*, IEEE Trans. Geosci. Remote Sensing, 48 (2010), pp. 1128–1137.
[38] F. S. M. W. L. Lo Monte and D. Erricolo, *RF tomography for below-ground imaging of extended areas and close-in sensing*, IEEE Geosci. Remote Sensing Lett., 7 (2010), pp. 496–500.
[39] K. J. Langenberg, M. Brandfass, K. Mayer, T. Kreutter, A. Brüll, P. Felinger, and D. Huo, *Principles of microwave imaging and inverse scattering*, EARSeL Adv. Remote Sens., 2 (1993), pp. 163–186.
[40] S. J. Norton and M. Linzer, *Backprojection reconstruction of random source distributions*, J. Acoust. Soc. Amer., 81 (1987), pp. 977–985.
[41] D. W. O'Hagan and C. J. Baker, *Passive bistatic radar (PBR) using FM radio illuminators of opportunity*, in Proceedings of the IEEE Radar Conference, Rome, Italy, 2008, pp. 1–6.
[42] D. Poullin, *Passive detection using digital broadcasters (DAB, DVB) with COFDM modulation*, IEE Proceedings of Radar, Sonar and Navigation, 152 (2005), pp. 143–152.
[43] M. J. Prickect and C. C. Chen, *Principles of inverse synthetic aperture radar*, in Proceedings of the EASCON, 1980, pp. 340–345.
[44] M. I. Skolnik, *Introduction to Radar Systems*, 3rd ed., McGraw–Hill, New York, 2008.
[45] D. K. P. Tan, H. Sun, Y. Lu, M. Lesturgie, and H. L. Chan, *Passive radar using global system for mobile communication signal: Theory, implementation and measurements*, IEE Proceedings of Radar, Sonar, and Navigation, 152 (2005), pp. 116–123.
[46] K. Voccola, B. Yazici, M. Cheney, and M. Ferrara, *On the equivalence of the generalized likelihood ratio test and backprojection method in synthetic aperture imaging*, in SPIE Defense and Security Conference, (Orlando, FL), Vol. 7335, SPIE, Bellingham, WA, 2009, pp. 73350I-1–73350I-10.
[47] L. Wang, I. Y. Son, and B. Yazici, *Passive imaging using distributed apertures in multiple scattering environments*, Inverse Problems, 26 (2010), 065002.
[48] L. Wang and B. Yazici, *Passive radar imaging of moving targets with sparsely distributed receivers*, in Proceedings of the 6th IEEE Sensor Array and Multichannel Signal Processing Workshop (SAM 2010), Israel, 2010, pp. 257–260.
[49] L. Wang and B. Yazici, *Passive radar imaging of moving targets using distributed apertures*, in Proceedings of the SPIE Symposium on Defense, Security and Sensing (Orlando, FL), Vol. 8021, SPIE, Bellingham, WA, 2011, pp. 80211F-1–80211F-11.
[50] Y. Wu and D. C. Munson, *Multistatic synthetic aperture imaging of aircraft using reflecting television signals*, in Proceedings of the SPIE Symposium on Algorithms for Synthetic Aperture Radar Imagery, Vol. 4382, SPIE, Bellingham, WA, 2001, pp. 1–12.
[51] Y. Wu and D. C. Munson, *Wide-angle ISAR passive imaging using smoothed pseudo Wigner-Ville distribution*, in Proceedings of the IEEE Radar Conference, IEEE, Washington, DC, 2001, pp. 363–368.

[52] C. E. Yarman, L. Wang, and B. Yazici, *Doppler synthetic aperture hitchhiker imaging*, Inverse Problems, 26 (2010), 065006.
[53] C. E. Yarman and B. Yazici, *Synthetic aperture hitchhiker imaging*, IEEE Trans. Image Process., 17 (2008), pp. 2156–2173.
[54] C. E. Yarman, B. Yazici, and M. Cheney, *Bistatic synthetic aperture radar imaging for arbitrary flight trajectories*, IEEE Trans. Image Process., 17 (2008), pp. 84–93.